JMEPEG (2022) 31:5161–5188
https://doi.org/10.1007/s11665-022-06667-x

1059-9495/$19.00

REVIEW

Residual Stress and Distortion during Quench Hardening of Steels: A Review

Augustine Samuel and K. Narayan Prabhu

Submitted: 23 June 2021 / Revised: 17 December 2021 / Accepted: 5 January 2022 / Published online: 10 March 2022

Quench hardening is a widely used heat treatment process for achieving better mechanical properties in carbon steels. However, when high quench-sensitivity steel components having thin sections are quenched, they may get distorted due to thermal and phase transformation stresses. Appropriate steps have to be taken to minimize residual stresses and distortion during quenching operation in the heat-treating industry. Many factors such as quenchant type, quench severity, quenching process variables, the geometry of the component, and material properties significantly affect the evolution of residual stresses. The heat transfer from the metal surface to the quench medium is the critical physical phenomenon that drives the microstructure evolution and residual stresses during quenching. The nonuniformity in heat transfer between the heated metal and the quench medium is the key source of residual stress development in the quenched material. Modeling and simulation of the quenching process can predict the residual stress distribution in the quenched sample and the evolution of quench cracks and component failure. Optimizing quenching process conditions and selecting appropriate quenchants minimize residual stresses and distortion. One of the requirements for improving the accuracy of simulation models is the use of reliable spatiotemporal heat transfer boundary conditions. The present review addresses the evolution of residual stresses during quenching, factors affecting residual stresses such as geometry and section thickness of the quenched part, cooling uniformity, quenchant selection, and the interrelation between heat transfer and residual stresses. The methods to minimize residual stress and distortion in quenched parts are discussed.

Keywords residual stress, distortion, quench hardening, quenchant, heat transfer, cooling uniformity

1. Introduction

Quench heat treatment is a commonly used process of hardening steel. In this process, the components are heated to a higher temperature for a certain length of time until a homogeneous single-phase solid solution is attained and rapidly cooled in a quenching medium. The hardening is achieved by arresting the diffusion motion of atoms and attaining a metastable structure. In doing so, the phase transformation of the parent phase to stable product phases is avoided. In steels, the transformation from the austenite to the metastable martensite phase is desired to achieve higher hardness in the material. Apart from the conventional hardening, quenching is applied in post-surface heat treatment operations such as induction, flame, and laser hardening or following the thermochemical treatments

Augustine Samuel and **K. Narayan Prabhu**, Department of Metallurgical and Materials Engineering, National Institute of Technology Karnataka, Surathkal, Mangalore 575025, India. Contact e-mails: augustinesamuel2511@gmail.com, knprabhu.nitk@gmail.com, knprabhu@nitk.edu.in.

List of symbols

Notations

T	Temperature (°C)
ΔT	Temperature difference (°C)
t	Time (s)
q	Heat flux (W/m^2)
h	Heat transfer coefficient (W/m^{2}K)
L	Length (m)
ϕ/D	Diameter (m)
r	Radius (m)
z	Axial distance (m)
σ_{l}, σ_{θ}, σ_{r}	Stresses in longitudinal, tangential (hoop) and radial directions (N/m^2)
σ_f, σ_o	Flow stress, yield strength (N/m^2)
E	Elastic/Young's modulus (N/m^2)
H_k	Plastic hardening modulus (N/m^2)
K_k	Strain hardening parameter
υ	Poisson's ration
α_k	Thermal expansion coefficient (K^{-1})
$\rho, \rho_{\mathrm{l}}, \rho_{\mathrm{v}}$	Density, density of liquid and vapor phases (kg/m^3)
C, C_{pl}, C_{pv}	Specific heat, specific heat capacity of liquid and vapor phases (J/kg K)
$\lambda, \lambda_l, \lambda_v$	Thermal conductivity, thermal conductivity of liquid and vapor phase (W/m K)
Q	Internal heat generation/latent heat (J/kg)
Δh	Enthalpy change (J/kg)
ξ	Phase fraction
Δ_k	Dilatational strain
δ_{ij}	Kronecker's delta

σ_{ij}	Stress tensor (N/m^2)
ε_{ij}	Strain tensor
σ_{mm}	Diagonal elements of the stress tensor (N/m^2)
Φ	Yield functional
D_{ijkl}	Elastoplastic constitutive strain tensor (N/m^2)
g	Acceleration due to gravity (m/s^2)
h_{fg}	Latent heat evolved due to liquid–vapor phase change (J/kg)
D_o	Length scale for vapor bubble diameter (m)
μ_l, μ_v	Viscosity of liquid, vapor (Pa.s)
γ_{lv}	Surface tension of liquid (N/m)
γ_{sv}	Surface energy of solid (N/m)
γ_{sl}	Solid/liquid interfacial tension (N/m)
θ_e	Equilibrium contact angle (°)
CR	Cooling rate (°C/s)
H, H_p	Grossmann quench severity, local Grossmann quench severity (m^{-1})
α	Thermal diffusivity (m^2/s)
E_Z	Normalized energy extracted along the z direction
T_{sat}	Saturation temperature of the liquid (°C)
ΔT_{sub}	Difference between saturation and bath temperature of the quench medium (°C)
T_b	Bath temperature (°C)
Ja	Jakob number
Pe	Peclet number
Bi	Biot number
M_S	Martensite transformation start temperature (°C)
M_F	Martensite transformation finish temperature (°C)

Operators

$\dot{}$	Time derivative
$\nabla()$	Gradient operator
$\nabla.()$	Divergence operator

Abbreviations

FE/FEM	Finite element/finite element method
HTC	Heat transfer coefficient
IHCP	Inverse heat conduction problem
CFD	Computational fluid dynamics
LFP	Leidenfrost point
MHF	Minimum heat flux
CHF	Critical heat flux
ANN	Artificial neural network
PAG	Polyalkylene glycol
PVP	Polyvinyl pyrolidone
MWCNT	Multiwalled carbon nanotubes
DW	Distilled water
SO	Soybean oil
ESBO	Epoxidized soybean oil
FAME	Fatty acid methyl esters

like carburizing and nitriding. The rapid cooling is performed by direct immersion into the quench medium, or the fluid is brought in contact with the heated metal. The former quenching process is known as immersion quenching, while the latter are quenching processes such as spray quenching, film quenching, and gas quenching (Ref 1).

The heat transfer during quenching drives the microstructural evolution and development of stress and strain in the material. Nonuniform heat transfer at the surface creates a thermal gradient on the surface and within the quenched sample. Stresses are developed due to nonuniform plastic yielding due to thermal and transformation stresses. Thermal stresses result from unequal contraction or shrinkage due to the differential coefficient of thermal expansion. Transformation stresses result from volume expansion due to phase change from the parent to product phases. In addition to it, phase transformation induces stress due to transformation plasticity (TRIP). The resultant of these stresses is usually contained in the material as residual stress. If the stress surpasses the yield strength of the material, the material starts changing its shape or starts cracking (Ref 2). Quench distortion and cracking are the two major defects of the quenching process. In steels, the volume expansion due to the transformation from austenite to martensite is the major contributor to quench defects (Ref 3).

Residual stresses and distortion during quenching are the primary causes for the rejection or rework of the components. Post-heat treatment operations are necessary to minimize residual stresses or distortion, making the process expensive (Ref 2). In some applications, residual stress in the material is advantageous for enhancing the component's life span. High surface compressive residual stress improves fatigue life, wear, and corrosion resistance of the component (Ref 4-7), whereas high tensile residual stresses developed in the material due to quenching lead to dimensional instability during the service life of the component (Ref 8). Therefore, analyzing residual stress distribution in the material during quenching is essential.

Residual stresses and distortion can be controlled by optimizing the quenching process conditions such as the quenchant type, bath temperature, method of quenching, and agitation. The nonuniformity in heat transfer is a significant cause of the unequal residual stress distribution and distortion (Ref 9). The nonuniformity arises due to the various stages of heat transfer and due to the rewetting phenomena occurring at the metal/quenchant interface during quenching. Accurate boundary heat transfer conditions will improve the accuracy of the quenching process simulation and thus improve the prediction accuracy of residual stresses and distortion (Ref 10). According to Heat Treating Industry Vision, 2020 and Heat treating Technology Roadmap 200 established by the ASM Heat Treating Society and Materials Treating Institute, the objectives of zero distortion, zero-dispersion of quality, and zero pollution have to be achieved (Ref 11, 12). The Vision 2020 Research and Development plan (1999) put forward by the Heat Treating Society had three broad research proposals: (1) equipment and materials for heat treatment, (2) the heat-treating technology needs, and (3) reduction in energy consumption and pollution control. The heat-treating technology needs consisted goals of developing quenching models highlighting the following features:

1. Development of a robust model to compute heat transfer coefficient (HTC) based on the time-temperature data that takes care of geometry and surface finish of the component.
2. A scaling rule to estimate HTC for various part dimension
3. To create a database of HTC and empirical relationships

4. Combining CFD modeling for accurate prediction of flow pattern and temperature-time data

The goal of reduction in energy consumption and pollution control involved (1) developing high-intensity heating and cooling system, (2) finding an alternative quenchant to mineral oil, (3) recover, recycle and reuse of waste generated, and (4) finding an alternative to NO_3/NO_2, CN, barium salts, and solvent cleaner (Ref 13, 14). The alternative quenchants developed should minimize the residual stress and distortion in the heat treated component.

2. Theory of Evolution of Residual Stresses during Quenching

Krause and Juhe (Ref 15) broadly classified residual stress as stresses of 1st, 2nd, and 3rd kind according to their homogeneity and the scale of occurrence. Residual stress of the 1st and 2nd kinds is macroscopic. The first kind of residual stresses are equilibrated across the whole body or several grains, and the second kind is equilibrated along one grain. The 3rd kind of stress is microscopic and is equilibrated in a sub-granular region. Any disturbance to the equilibria of the first and the second kind will cause considerable distortion in the material, whereas, for the third kind, any change in equilibrium will not cause any visible dimensional changes. The total residual stress across a distinct region in a body is equal to the resultant of all three kinds of residual stresses.

Residual stress during quenching occurs due to the spatial and temporal variation of temperature that leads to a large thermal gradient in the quenched body. The thermal gradient leads to unequal contraction and nonuniform microstructure. Unequal contraction leads to the evolution of thermal strain, and nonuniform microstructure leads to phase transformation strain. Residual strains are a combination of thermal and transformation strains. During rapid cooling of a cylindrical specimen, biaxial longitudinal and tangential stresses are developed at the surface and are compensated by the core's triaxial longitudinal, tangential, and radial stresses. Metallic material generally exhibits an elastic-plastic deformation behavior, and the material's yield stress controls the onset of plastic deformation. The yield stress is a function of temperature and decreases with increasing temperature. The material is said to deform plastically when the effective or local equivalent stress is equal to or greater than the yield stress at that particular temperature. The equivalent stress is found using any of the failure hypotheses for the ductile material, usually the Von Mises yield criterion (Ref 16).

2.1 Residual Stresses Due to Thermal Shrinkage

Considering a transformation-free cylindrical specimen, the residual stress occurs due to the spatial variation in the cooling rate. The surface cools faster than the core as soon as the

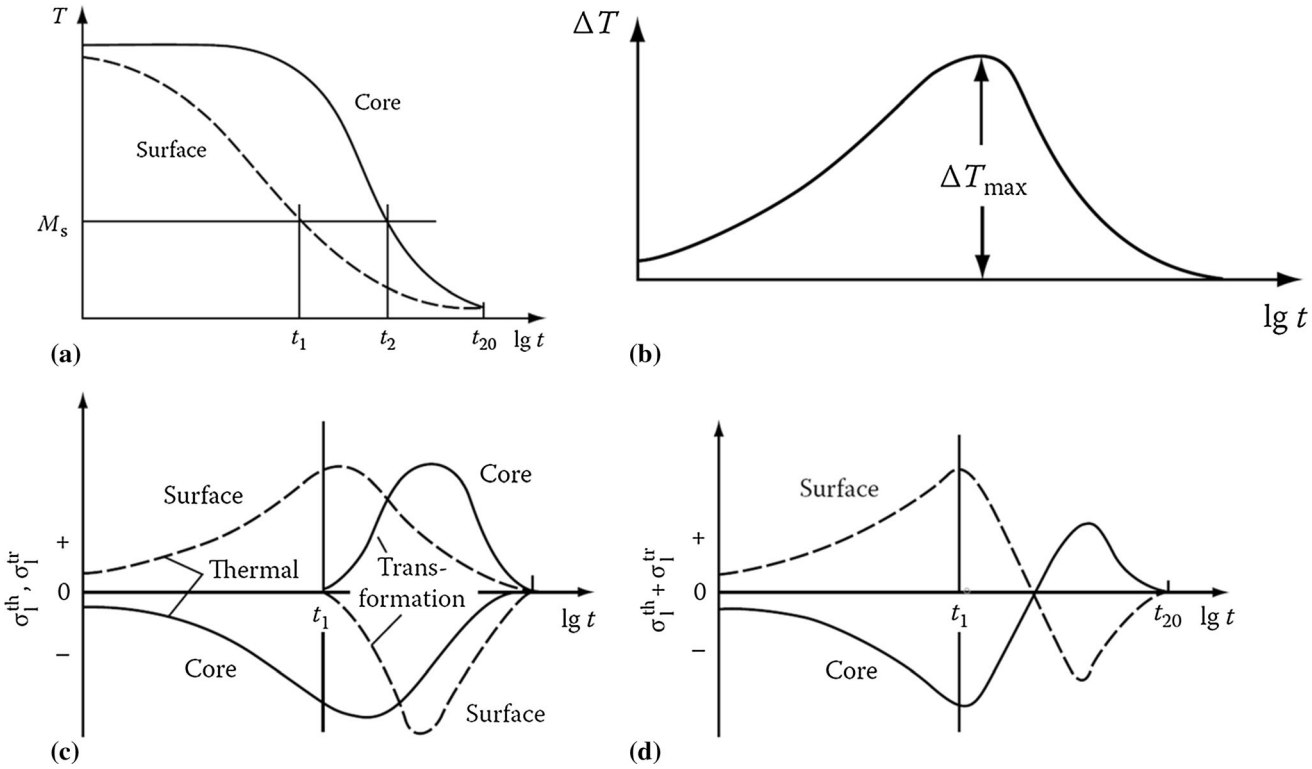

Fig. 1. (a) Cooling curves of a cylindrical specimen during quenching, (b) temperature difference between the surface and core as a function of time, (c) longitudinal thermal and transformational residual stresses evolved during quenching considering ideal linear elastic material, (d) resultant longitudinal residual stress variation due to combined thermal and transformational stresses (Ref 16). Copyright 2010 from Residual Stresses after Quenching by V. Schulze, O. Vohringer, E. Macherauch. Reproduced by permission of Taylor and Francis Group, LLC, a division of Informa plc

cylinder is quenched. The thermal contraction at the surface causes tensile stress. Opposing compressive stress is evolved at the core to balance the tensile stress. After a specific time, when the difference in temperature between the surface and core reaches a maximum value (ΔT_{max}), as shown in Fig. 1(b), the cooling rate at the core becomes higher than that of the surface. The tensile stress acts on the core and is balanced by compressive stresses at the surface. The new stresses lead to a decrease in the preceding stresses at both surface and the core. If the stresses are elastically accommodated, then the magnitude of the stress at both regions decreases to zero. However, the residual stress remains in the specimen due to nonuniform plastic deformation occurring during cooling. At any point of time during cooling, if the local equivalent residual stress exceeds the yield strength, plastic deformation occurs. The plastic deformation at the surface and core occurs at different times due to the variation in the cooling rate. At the end of cooling, plastic extension and compression remain at the surface and core, respectively, which causes residual stress to be compressive and tensile at the surface and core. Therefore, during cooling, the inversion of stress takes place from tensile to compressive at the surface and vice versa at the core (Ref 17).

2.2 Residual Stress Due to Phase Transformation

The phase transformation of austenite to martensite or any other product phases causes an increase in the volume. As a result, compressive stresses are evolved in the region of transformation. During quenching, the surface of the cylinder being first to cool transforms into martensite, and compressive stresses are developed in this region. The untransformed core balances the compressive stresses by developing tensile stresses. As the cooling time progresses, the core transforms to martensite, and the surface transformation is nearly complete. The compressive stresses are established at the core and balanced by developing tensile stresses at the surface. Hence, the pre-existing stresses at both surface and core are reduced by the newly established stresses. The plastic deformation due to phase transformation at the surface and core varies in magnitude and opposes in nature. At the end of cooling, residual stress remains compressive at the core and tensile at the surface (Ref 16).

2.3 Residual Stress Due to Combined Thermal and Phase Transformation Stresses

In the case of the combined thermal and phase transformation stresses, the compressive stresses produced by phase transformation will shift the pre-existing stress in the negative direction. The untransformed region will produce stress in the positive direction. Residual stress evolves in three consecutive stages. Pure thermal stress acts on the material at the initial stage as there is no austenite phase transformation. The surface is the first to cool and develops tensile stress due to thermal shrinkage. The core develops compressive stress to balance the tensile stress at the surface. The second stage is when the temperature reaches the Martensite start (M_S) point. Transformation of austenite to martensite will cause compressive stress due to volume expansion and the transformation-induced plasticity (TRIP). Transformation at the surface starts earlier than the core, as shown in Fig. 1(a). In the final stage, the core starts to transform, and the transformation at the surface is almost complete. Phase transformation will cause a rapid decrease and increase of stress in the reverse direction at the surface and the core. The irregular or nonuniform plastic deformation at the surface and the core will decide the magnitude of residual stress at the end of cooling. The variation of longitudinal residual stresses during cooling for an ideal elastic material is shown in Fig. 1(c) and (d).

The final residual stress distribution in the cylinder depends on the initiation time of transformation at the surface and core, i.e., whether the start of transformation at the surface and core will occur before/after or at the same time as that of inversion of residual thermal stress. The combinations will yield different residual stress distributions. Therefore, the residual stresses due to combined thermal and transformational stresses can be broadly classified into thermal, transition, and transformation types, as shown in Fig. 2. In the thermal type, the surface is

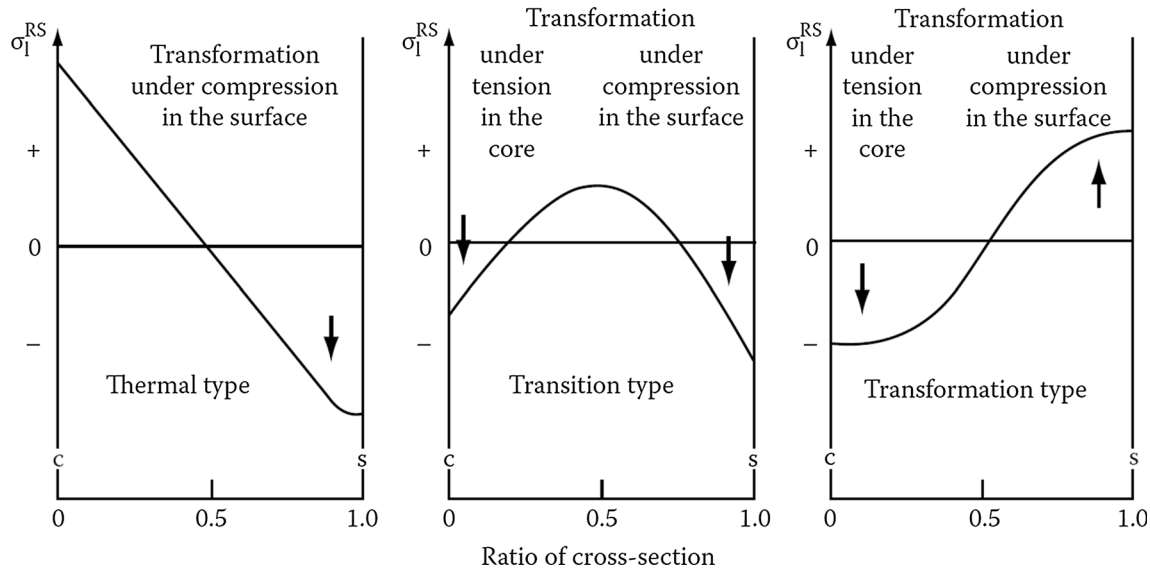

Fig. 2. Longitudinal residual stress distribution in the radial direction of a cylindrical steel specimen due to combined thermal and transformation stresses [16]. Copyright 2010 from Residual Stresses after Quenching by V. Schulze, O. Vohringer, E. Macherauch. Reproduced by permission of Taylor and Francis Group, LLC, a division of Informa plc

under compression, and tensile stresses act on the core, whereas the surface is under tension, but compressive stresses act on the core for the transformation type. In the transition type, both surface and core are under compression, and the tensile stress maxima occur between the surface and the core. Increasing the section thickness will change the residual stress distribution from thermal to transformation type, whereas increasing the quench severity with a smaller diameter specimen will change the residual stress distribution from transformation to thermal type (Ref 16).

2.4 Transformation-Induced Plasticity (TRIP)

Transformation plasticity is the excessive plastic strain occurring in the softer austenite phase during cooling due to the interaction between the thermal and transformation stresses. TRIP can be explained by the dilatometry experiment where the specimen undergoing phase transformation from austenite to product phases is subjected to uniaxial tensile or compressive stresses. The investigation indicates that with an increase in tensile or compressive loading, the transformation strain is enhanced in the direction of loading. TRIP occurs even when the local equivalent stress is lower than the yield strength of the austenite phase. Phase transformation occurring in a micro-region will result in a change of shape or volume. The neighboring softer parent phase accommodates the incompatibility or misfit due to phase change by plastic yielding. The plastic deformation causes an irreversible strain, also known as eigen strain, that creates an eigen stress. Eigen stress is defined as self-equilibrated internal stress occurring due to one or several eigen strains in the body without any influence of external force or constraints. The magnitude of eigen stress varies within the body (Ref 17).

The evolution of TRIP can be explained by two competing theories or mechanisms (Ref 2, 17-19):

1. Greenwood and Johnson mechanism: This theory suggests that during phase transformation under the influence of stress in a micro-region, the softer parent phase (austenite) deform plastically in the region near the progressing transformation front, causing an irreversible strain. The mechanism is applicable for both diffusional and displacive transformation.
2. Magee's mechanism: This theory suggests that in an iron-based alloy, the transformation from austenite (FCC) to martensite (BCT) occurs through 24 types of variants, each with its lattice orientation relationship. The variants are described by the dilatational strain perpendicular to the habit plane and the shear strain parallel to the habit plane. Only those variants that are favorably oriented in the applied stress direction will nucleate. According to this mechanism, deformation of austenite due to martensitic transformation is considered anisotropic and attains a maximum value in the applied stress direction.

The contribution of both the mechanism describes transformation plasticity during martensitic transformation. During the transformation, only those variants oriented in the direction of applied stress nucleates. The nucleation leads to anisotropic deformation of austenite, causing TRIP strain. The value of TRIP strain increases in the applied stress direction and achieves a maximum value when the applied stress reaches the yield strength of austenite. As the transformation progresses further, the TRIP strain decreases in the direction of applied stress due to stress relaxation resulting from plastic deformation. As a result, the variants oriented in the internal stress direction nucleate rather than the applied stress. The applied stress is the thermal stress developed during quenching. Magee's mechanism is dominant during the initial stages of transformation, and in the later stages, the Greenwood-Johnson mechanism becomes dominant (Ref 17).

3. Modeling of Quenching Process

The quench hardening process is a coupled phenomenon that involves the simultaneous occurrence of various physical events and mutual interaction between the events, as shown in Fig. 3. Heat transfer (Temperature field), phase transformation (Metallurgical field), and stress/strain evolution (Mechanical field) co-occur such that the occurrence of one physical event affects the occurrence of another. Interaction between these physical events occurs by mutual sharing of one or more state variables. Heat transfer from the specimen to the quench medium is the driving force for all other physical events. The transient temperature field causes phase transformation in the specimen, and the presence of thermal gradient causes uneven contraction leading to the evolution of thermal strain. The phase transformation is associated with the latent heat evolution, which alters the temperature field. In addition, phase transformation alters the mechanical field by the development of transformation strain. The development of

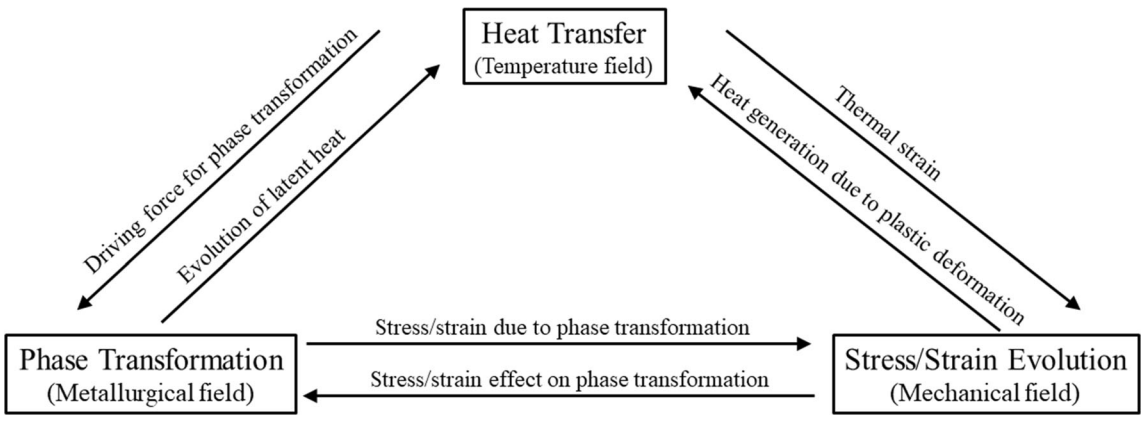

Fig. 3. Coupled interaction between various fields during the quenching process (modified and redrawn from Ref 2)

stress/strain in the specimen's body leads to local plastic deformation, which releases the stored strain energy in the form of heat and, hence, affects the temperature field. Since the plastic deformation occurring during the quenching process is very small, the heat generated due to plastic deformation is usually neglected in quenching simulation. The mechanical field also influences the metallurgical field. The stress/strain developed in the material affects the critical transformation temperatures and the transformation kinetics.

3.1 Modeling of Temperature Field

The transient Fourier heat conduction equation (Eq 1) is the governing equation for the determination of temperature distribution in the specimen during quenching.

$$\rho C\dot{T} = \nabla.(\nabla(\lambda T)) + Q \qquad \text{(Eq 1)}$$

where ρ, C, and λ are temperature-dependent density, specific heat, and thermal conductivity of the phase mixture in a polycrystalline specimen, respectively. Q is the internal heat generation term due to latent heat evolution during phase transformation.

The thermophysical properties ($P(T, \xi_k)$) of the phase mixture are estimated by the linear rule of mixtures.

$$P(T, \xi_k) = \sum_{k=1}^{N} P_k \xi_k \qquad \text{(Eq 2)}$$

P_k is the property of the kth constituent phase and ξ_k is the volume fraction of the kth phase.

The rate of internal heat generation ($\dot{Q}$) is estimated as shown below.

$$\dot{Q} = \Delta h_k \dot{\xi}_k \qquad \text{(Eq 3)}$$

Δh_k is the change in enthalpy per unit volume at constant pressure and $\dot{\xi}_k$ is the phase transformation rate of the kth phase.

Another method of incorporating latent heat into the heat conduction equation is in the form of fictitious specific heat (C^*).

$$C^* = \sum_{k=1}^{N} C_k \xi_k + \Delta h_k \frac{\mathrm{d}\xi_k}{\mathrm{d}T} = C + \frac{\dot{\xi}_k}{\dot{T}} \Delta h_k \qquad \text{(Eq 4)}$$

The boundary conditions and initial condition for solving the heat conduction equations are as follows:

The heat flux for the surfaces in contact with the quench medium is evaluated by:

$$q(T_s, T_\infty) = h(T_s)(T_s - T_\infty) \qquad \text{(Eq 5)}$$

where T_S and T_∞ are the surface temperature of the specimen and ambient or the bath temperature of the quench medium and h (T_S) is the surface temperature-dependent heat transfer coefficient.

It is assumed that surfaces not in contact with the quench medium or symmetry surface are insulated, i.e.,

$$\lambda \frac{\partial T}{\partial n} = 0 \qquad \text{(Eq 6)}$$

where n is the surface normal.

$$\text{At time} \quad t = 0,\ T(x, y, z, t) = T_0 \qquad \text{(Eq 7)}$$

T_0 is the austenitizing temperature (Ref 2, 17-19).

3.2 Modeling of Metallurgical Field

The phase transformations in steels are classified as diffusion-controlled (transformation from austenite to ferrite, pearlite, and bainite) and diffusionless or displacive (martensitic transformation) and occur under anisothermal conditions. The diffusion-controlled phase transformation involves an initial incubation period and subsequent growth stage. The incubation period is calculated using Scheil's additivity rule (Ref 20-22). According to this rule, the incubation period is complete, or the phase transformation begins when Schiel's sum (S) equals unity. Schiel's sum is expressed as shown below.

$$S = \sum_{j=1}^{n} \frac{\Delta t_j}{\tau_s(T_j)} \approx 1$$

where Δt_j is the time step increment and $\tau_s(T_j)$ is the isothermal time required for the start of transformation at the present temperature T_J.

After the completion of the incubation period, the growth kinetics of the diffusion-controlled phase transformation is modeled using the Johnson–Mehl–Avarami–Kolmogorov (JMAK) equation (Ref 23).

$$\xi_k^{t+\Delta t} = \xi_k^{\max}\left(\xi_\gamma^t - \xi_k^t\right)\left(1 - \exp\left(b_k(T)(\tau + \Delta t)^{n_k(T)}\right)\right) \qquad \text{(Eq 9)}$$

where $\xi_k^{t+\Delta t}$ is the volume fraction of the product phase in the present time step. ξ_γ^t and ξ_k^t are the volume fractions of austenite and product phase at the previous time step. $\xi_k^{\max}$ is the maximum volume fraction of the product phase. For complete pearlitic or bainitic transformation, $\xi_k^{\max}$ is equal to the available volume fraction of austenite at the beginning of the transformation.

For proeutectoid transformation, the maximum volume fraction of ferrite ($\xi_\alpha^{\max}$) is calculated from the equilibrium phase diagram using lever rule.

τ is the fictitious time calculated based on the volume fraction of the kth product phase in the previous time step.

$$\tau = \left(\frac{-\ln(1 - \xi_k(t)}{b_k(T)}\right)^{\frac{1}{n_k(T)}} \qquad \text{(Eq 10)}$$

τ is incremented by the time step Δt to obtain the newly transformed volume fraction. $b_k(T)$ and $n_k(T)$ are the temperature-dependent time coefficient and exponent, respectively, calculated from the isothermal transformation diagram.

The diffusionless or martensitic transformation is modeled using the Koistinen–Marburger (KM) equation (Ref 24).

$$\xi_m = \xi_\gamma(1 - \exp(-\Omega(M_s - T))) \qquad \text{(Eq 11)}$$

ξ_m is the volume fraction of martensite at the present step, ξ_γ is the volume fraction of austenite, Ω is a constant whose value is taken as 0.011 regardless of chemical composition for most of the steels, and M_s is the martensite start temperature (Ref 2, 19).

3.2.1 Prediction of Flow Stress of the Phase Mixture. Due to the continuous evolution of the microstructure during phase transformation, the mechanical properties of the phase mixture, such as the flow stress, continuously change.

The linear rule of the mixture is the most common method of calculating the flow stress. According to this rule, the overall flow stress is expressed as:

$$\sigma_f = \sum_{k=1}^{p} \xi_k \sigma_o^k \quad \text{(Eq 12)}$$

where σ_o^k is the yield strength of the kth constituent phase.

The linear mixture rule works well when the coexisting phases' hardness is comparable. When the coexisting phases have a significant difference in hardness, Reuss, Leblond, Voigt, and Geijsalers models are used (Ref 2).

The flow stress equation considering the effect of plastic memory loss is illustrated by (Ref 19):

$$\sigma_f = \sum_{k=1}^{p} \xi_k \sigma_o^k + \sum_{k=1}^{p} \xi_k \kappa_k H_k = \sigma_o + \sum_{k=1}^{p} \xi_k \kappa_k H_k \quad \text{(Eq 13)}$$

κ_k is the strain hardening parameter that accounts for the plastic memory loss during transformation, and H_k is the plastic hardening modulus. The strain hardening parameter is calculated through transformation progress.

$$\dot{\kappa}_{k_{(t+\Delta t)}} = \int_{t=0}^{t} \left(\dot{\bar{\varepsilon}}^p - \frac{1}{\xi_k} \dot{\xi}_k \kappa_{k_{(t)}} \right) \mathrm{d}t \quad \text{(Eq 14)}$$

$\bar{\varepsilon}^p$ is the effective plastic strain.

3.3 Modeling of Mechanical Field

Due to different physical events, the overall strain rate (increment in strain) is decomposed into strain rate terms. The total strain rate is expressed as shown below.

$$\dot{\varepsilon}_{ij} = \dot{\varepsilon}_{ij}^e + \dot{\varepsilon}_{ij}^p + \dot{\varepsilon}_{ij}^{th} + \dot{\varepsilon}_{ij}^{pt} + \dot{\varepsilon}_{ij}^{tr} \quad \text{(Eq 15)}$$

where $\dot{\varepsilon}_{ij}^e$, $\dot{\varepsilon}_{ij}^p$, $\dot{\varepsilon}_{ij}^{th}$, $\dot{\varepsilon}_{ij}^{pt}$, $\dot{\varepsilon}_{ij}^{tr}$ are the elastic, plastic, thermal, phase transformation, and transformation plasticity strain rates, respectively.

The stress field is most commonly simulated, considering the elastoplastic (strain rate-independent) model. For defining an elastoplastic problem in a multiaxial case, three fundamental principles have to be described, viz., (1) yield function to determine the yield surface, (2) flow rule to determine the plastic flow path, and (3) hardening rule to determine the expansion/shift of yield surface (Ref 25). For ductile materials such as steel, von Mises yield criterion is used with Prandtl-Reuss flow and isotropic or kinematic hardening rules.

The individual strain rate terms are calculated using Eq 16, 17, 18, 20, and 22 (Ref 2, 19).

$$\dot{\varepsilon}_{ij}^e = \frac{1}{E}\left[-\left(\frac{(1+\upsilon)\sigma_{ij} - \delta_{ij}\upsilon\sigma_{mm}}{E} \right)\dot{E} + \left(\sigma_{ij} - \delta_{ij}\upsilon\sigma_{mm}\right)\dot{\upsilon} + (1+\upsilon)\dot{\sigma}_{ij} - \delta_{ij}\upsilon\dot{\sigma}_{mm} \right] \quad \text{(Eq 16)}$$

E and υ are the elastic modulus and Poisson's ratio, respectively. Both the parameters are dependent on temperature and phase fraction of product phases.

$$\dot{\varepsilon}_{ij}^{th} = \sum_{k=1}^{p} \left[\dot{\xi}_k \int_0^T \alpha_k . \mathrm{d}T + \xi_k \alpha_k \dot{T} \right] \quad \text{(Eq 17)}$$

α_k is the thermal expansion coefficient of the kth phase.

$$\dot{\varepsilon}_{ij}^{pt} = \sum_{k=1}^{p-1} \frac{1}{3} \delta_{ij} \Delta_k \dot{\xi}_k \quad \text{(Eq 18)}$$

Δ_k is the structural dilatation due to austenite transformation to kth product phase.

$$\Delta_k = \frac{\rho_\gamma}{(\rho_k - \rho_\gamma)} \quad \text{(Eq 19)}$$

where ρ_γ and ρ_k are densities of austenite and kth product phase, respectively.

$$\dot{\varepsilon}_{ij}^{tr} = \frac{3}{2} K_k \dot{\xi}_k (1 - \xi_k) S_{ij} \quad \text{(Eq 20)}$$

K_k is known as the transformation plasticity constant.

$$K_k = k \frac{\Delta_k}{\sigma_o^\gamma} \quad \text{(Eq 21)}$$

is the yield strength of the austenite phase, and the constant k value lies between 0.25 and 0.83.

$$\dot{\varepsilon}_{ij}^p = d\lambda \frac{\partial \Phi}{\partial \sigma_{ij}} \quad \text{(Eq 22)}$$

where Φ is the yield functional and $d\lambda$ is the plastic multiplier.

$$\Phi = F(\sigma_{ij}) - \left(\sigma_f(T, \xi_k, \bar{\varepsilon}^p)\right)^2 \quad \text{(Eq 23)}$$

$F(\sigma_{ij})$ is the applied stress state and σ_f is the variable flow stress.

$$\frac{\partial \Phi}{\partial \sigma_{ij}} = \frac{\partial F}{\partial \sigma_{ij}} \quad \text{and} \quad F(\sigma_{ij}) = \frac{3}{2} S_{ij} S_{ij} \quad \text{(Eq 24)}$$

S_{ij} is the deviatoric stress tensor.

$$S_{ij} = \sigma_{ij} - \frac{1}{3}\delta_{ij}\sigma_{mm} \quad \text{(Eq 25)}$$

To relate the stresses and strain rates, a hypoelastic equation is used as shown below (Ref 2).

$$\dot{\sigma}_{ij} = D_{ijkl}\dot{\varepsilon}_{kl}^e = D_{ijkl}\left(\dot{\varepsilon}_{ij} - \dot{\varepsilon}_{ij}^p - \dot{\varepsilon}_{ij}^{th} - \dot{\varepsilon}_{ij}^{pt} - \dot{\varepsilon}_{ij}^{tr} \right) \quad \text{(Eq 26)}$$

where D_{ijkl} is the elastoplastic constitutive tensor.

4. Application of Simulation to Quenching of Steels of Different Geometries Under Varying Quenching Conditions

Table 1 provides details of key research carried out applying FE simulation of quenching for steels of various compositions, geometries, and processing conditions.

The works on FE quenching simulation listed in Table 1 use a constant value of heat transfer coefficient (HTC) to calculate temperature distribution within the quenched specimen. In practice, the heat transfer during quenching occurs through various stages with significant differences in the HTC. The value of HTC varies continuously with time and space. Therefore, using a single value of HTC would not be justifiable to emulate the actual quenching process.

Table 1. FE quenching simulations applied to various heat treatment problems

Material type/geometry	Comment	References
AISI 1541 steel full-float truckload axle shaft	Induction heating and spray quenching was used to quench-harden the component. The effect of spray quenching rates on the residual stress distribution and distortion was analyzed. Due to its cyclic symmetry, a single 3D spline tooth of the axle shaft was used as the geometric model for simulation. Increasing quenching rates increased compressive residual stresses at the surface. Both the induction heating and quenching rates significantly affected the final residual stress state	26
316H stainless steel (1) cylinder (L/D ratio varied from 0.3 to 3.4) (2) sphere (r=15 mm)	High triaxial residual stresses are created over the volume of the specimen through spray water quenching. 2D axisymmetric models of the specimens were used for simulation. Via incremental hole drilling and neutron diffraction techniques, simulated residual stresses were compared with measured values. The magnitude and distribution of triaxial residual stresses were controlled by the surface heat transfer coefficient and the dimension of the specimen	27
Railway wheels made of low carbon bainitic-martensitic (LCBM) steels and pearlitic steels	Thermomechanical simulation involving the effect of martensite phase transformation on the residual stress distribution was carried out for the spray water quenching process. A 2D axisymmetric geometry was used for the simulation. A high level of compressive residual stresses on the wheel's rim could be developed by optimizing heat transfer coefficient and quenching process variables such as duration of quench and location of quenching	28
SAE 5120 Automotive gear	The FE simulation was used to model the carburization and quenching process of the gear and predict the final residual stresses and strains. The FE model was further used to evaluate the combined effect of residual stresses due to inhomogeneous phase transformation and applied torque on the gear tooth. The FE model helped refine the carburization and quenching process to improve compressive residual stresses on the surface to improve fatigue and wear resistance	29
Railway mono-block wheel	3D FE simulation using the whole geometry was developed. The residual stresses during the heat treatment process involving austenitizing, spray quenching, and annealing was analyzed. The magnitude of compressive residual stress distribution at the rim of the wheel is necessary to predict the component's fatigue life	30
Stainless steel plate (120 mm x 120 mm x 20 mm	The viscoelastic-plastic (strain rate dependent) model was applied to predict the residual stress distribution while quenching with 25% PAG polymer solution and mineral oil. The effect of transformation plasticity and strain rate on residual stresses was also included in the model. The residual strains produced while quenching with polymer quenchant were comparable with the mineral oil; however, the residual stresses were higher for the polymer quenchant	31
1080 carbon steel cylinder (ϕ38.1 mm × 76.2 mm)	Quenching was performed with water, 6%, and 14% aqueous polymer solutions. The FE simulation was used to predict the residual stress distribution in the steel cylinder while quenching in quenchants with different quench severities. The residual stresses were compressive at the surface and tensile at the core for all three quenchants. The magnitude of residual stresses was maximum for water. The increase in polymer concentration decreased residual stresses. The simulated results were in good agreement with the measured values by the x-ray diffraction technique	32
Cr12MoV steel cylinder (ϕ20 mm and L/D = 2.5)	The residual stress distribution while quenching the specimen with water and oil is simulated using the FE model. The surface heat transfer coefficient is estimated through the inverse heat conduction method. The residual stresses for both the quenchants were compressive at the surface and tensile at the core. Oil quenching showed lower residual stresses than water	33
1045 low alloy steel cylinder (ϕ 50 mm × 100 mm)	Quenching was performed with water and oil. The FE simulation of the quenching process was performed, incorporating the effect of stress on the transformation kinetics of ferrite and martensitic transformation. The accuracy of the prediction of residual stresses was improved. The model was validated through experimental measurement	34
Low alloy steel seamless tubes	The FE model was used to investigate the effect of discontinuous cooling during spray quenching of seamless tubes of various diameters. It was observed that the interrupted cooling had minimum or no effect on the evolution of residual stresses	35

Table 1. contiuned

Material type/geometry	Comment	References
Cylindrical specimen (ϕ60 mm × 240 mm) made of (1) Plain Carbon steel (0.4 wt.%C) (2)42CrMo and 40CrNiMo alloyed steels	The effect of incorporating transformation plasticity in the FE quenching simulation model while quenching in water was analyzed. The inclusion of transformation-induced plasticity effect in FE simulation had no effect on the final residual stress state for plain carbon steels with pearlitic matrix. In contrast, the effect was significant for the alloyed steels with bainitic and martensitic matrix. It was attributed to the higher transformation temperatures associated with the pearlitic matrix and lower transformation temperatures related to the bainitic and martensitic matrix. Higher transformation temperatures led to the relaxation of transformation-induced plastic deformation	36

In most cases, the final residual stress distribution was compressive at the surface and tensile at the interior. The magnitude of the residual stress depended on HTC. Higher HTC increased the residual stress, and decreasing HTC predicted a lower magnitude of residual stress. The stress distribution also depended on the section thickness of the specimen. For a given value of HTC in a cylindrical sample, a smaller diameter sample showed residual stress maxima (compressive and tensile) at the surface and core. As the section thickness increased, the tensile stress maxima shifted toward the half radius of the sample.

5. Rewetting Phenomena

The phenomenon of heat transfer from the surface of the specimen to the quench medium in the case of vaporizable quench media is a complex process involving conduction, convection, and radiation. The heat transfer occurs through three distinct stages: film boiling or vapor blanket, nucleate boiling, and convective cooling stages, as shown in Fig. 4. The film boiling stage occurs as soon as the hot metal is immersed in the quench medium. The quenchant in the vicinity of the heated specimen gets vaporized and forms a vapor envelope around the metal surface. The vapor film acts as an insulating layer, and the heat transfer occurs through radiation from the metal surface and conduction through the film. The vapor film remains stable until the surface temperature of the sample is greater than or equal to the Leidenfrost/ rewetting temperature. In the second stage, i.e., the nucleate boiling stage, the vapor film is broken, and tiny vapor bubbles form and ascend vigorously from the metal surface. The heat transfer in this stage is the maximum and occurs due to strong convective upward motion of the bubbles. The nucleate boiling stage ends when the metal surface temperature falls below the boiling temperature of the quenchant. In the final stage, i.e., the convective cooling stage, the quenchant is in direct contact with the metal surface, and the heat transfer occurs through convection. For each of the three stages, the value of the heat transfer coefficient differs significantly (Ref 37).

The transition from film boiling to nucleate boiling stage does not occur uniformly/instantaneously over the entire sample surface; instead, it happens over a period of time by forming a local wetting front. Usually, with a cylindrical sample, wetting front initiates at the bottom of the specimen as it is the first portion to cool and ascends toward the top (Fig. 5). As a result, the film boiling and nucleate boiling stages are simultaneous due to the wetting front movement. The significant difference in the heat transfer coefficients of film and nucleate boiling stages causes the oscillation in surface temperature leading to steep thermal gradients. The rewetting phenomenon is the primary source of nonuniformity or the spatial variation in heat transfer that leads to nonuniform hardening, residual stress, distortion and quench cracking (Ref 37, 38).

6. Estimating Boundary Conditions for the Simulation of Temperature Field

6.1 The Inverse Heat Conduction Method for Estimation of Heat Transfer Coefficient

The metal/quenchant interfacial heat transfer coefficient is generally estimated by solving the inverse heat conduction problem (IHCP). The IHCP method uses the temperature measurements taken within the sample to estimate the unknown boundary heat flux. The method is an iterative procedure wherein the objective function (S_{ts}) is minimized.

$$S_{ts} = \sum_{i=1}^{n} \sum_{j=1}^{m} \left(Y_{i,ts+j-1} - T_{i,ts+j-1}\right)^2 \quad \text{(Eq 27)}$$

The objective function is a least-square norm or the sum of the square of the error between the measured temperatures (Y) and calculated temperatures (T). The subscripts i, j, n, m, and ts represent the thermocouple number, time step number, total number of thermocouples, incremental time steps, and the current time step respectively. The total time steps (m) is taken as equal to future time+1. The future time steps are considered to account for the thermal gradient and obtain a smoothened output. In quenching problems where the temperature measurements are made near the surface, the future time step is taken as 4.

The calculated temperature is obtained by solving the transient Fourier heat conduction equation for m time steps. An initial guess of boundary heat flux is made, and the temperature is calculated at the location where the measurement was made. The objective function is then minimized by adapting a suitable iterative procedure. The assumed value of heat flux is incremented suitably in each iteration until a minimum value of the objective function is achieved. At the final iteration, the heat flux value for which the objective function is minimum is taken as the converged value of heat flux at that particular time step. Beck's nonlinear estimation method, Levenberg–Marquardt method, and conjugate gradient method are some of the

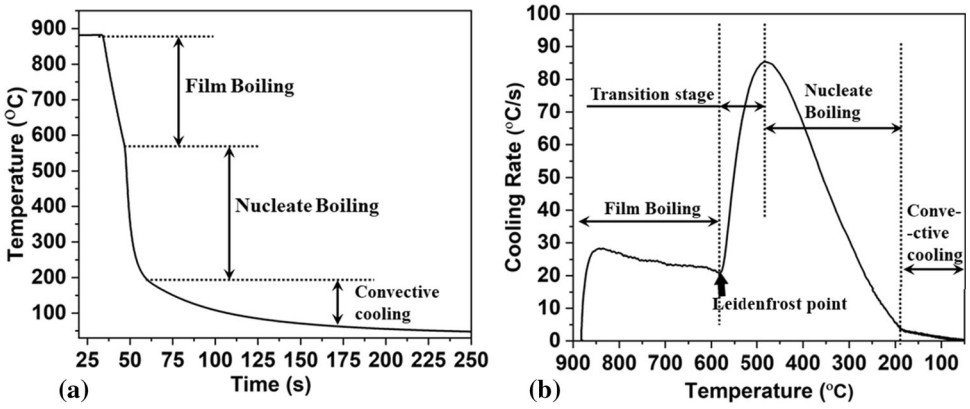

Fig. 4. (a) Cooling curve and (b) cooling rate v/s temperature curve during quenching indicating various heat transfer stages

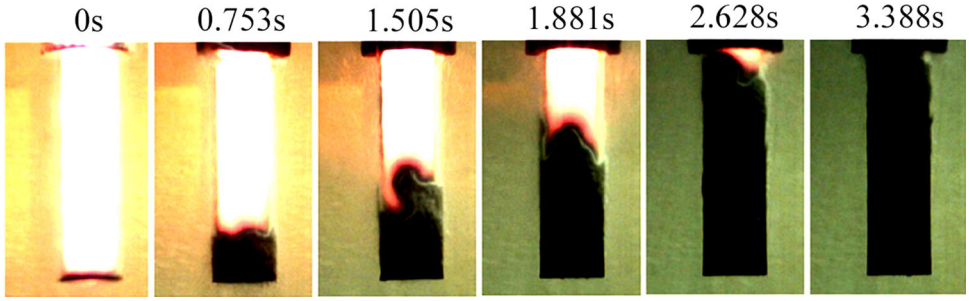

Fig. 5. Movement of the rewetting front during quenching of Inconel 600 standard probe in water. Reprinted by permission from Springer Nature Customer Service Centre GmbH: Springer Nature, *Metallurgical and Materials Transactions B*, Effect of Polymer Concentration on Wetting and Cooling Performance During Immersion Quenching, G. Ramesh, K.N. Prabhu, Copyright 2015 [38]

iterative techniques used to minimize the objective function. Figure 6 shows the various ways in which the output heat flux (q) is estimated. In case (1), a single value of boundary heat flux is assumed. In case (2), the boundary is divided into many numbers of unknown heat flux segments, and in case (3), the boundary heat flux is assumed to be a polynomial function of axial length (z). The estimated heat flux in case (1) is only temporally varying, whereas in case (2) and case (3), the variation is both spatial and temporal. In case (ii), each heat flux segment ($qi(t)$, i=1,2,3,4) is estimated for every time step, and in case (3), the parameters/coefficients (p_1, p_2, p_3, p_4) of the polynomial equation ($q(z,t)$) are estimated such that the objective function (S_{ts}) is minimized. The heat flux at any axial location (z) is obtained by substituting the coefficients in the polynomial equation. Figure 7 shows the corresponding heat flux output obtained with each of the three cases. The effect of rewetting phenomena on the uniformity of heat transfer is well captured when the spatial and temporally varying heat flux boundary condition is assumed. The boundary heat transfer coefficient calculated using the spatiotemporally varying heat flux would improve the accuracy of predicted temperature distribution in the quenched sample and improve the accuracy of predicting microstructure and residual stress distribution (Ref 39-42).

6.2 Use of Boiling Heat Transfer Correlations for the Estimation of Heat Transfer Coefficient

Jan and Mackenzie (Ref 43) applied CFD analysis incorporating the heat transfer correlations for the film boiling, transition, and nucleate boiling stages to predict the cooling curves within the quenched specimen. The authors proposed using local quench severity or local Grossman number (H_p) acting on an infinitesimal area of the quenched specimen. H_p varied with space, time, temperature, and material properties. The use of local quench severity would distinguish quench severity into separate heat transfer models, as shown in Fig. 8.

In the specimen, the heat transfer takes place by conduction. At the liquid/metal interface, conjugate heat transfer takes place. In the liquid, convection heat transfer, the energy exchange between liquid and vapor phase and latent heat absorption during phase change from liquid to vapor phase occurs. Except for the boiling model, all other heat transfer models are solved in commercial CFD software using the Eulerian method, where the mass/momentum and energy equations are solved. The boiling model is experimental-specific and requires calibration. The following empirical equations express the boiling heat transfer model:

Bromley's equation gives the heat transfer coefficient in the film boiling regime (Ref 44).

$$h = 0.62\left[\frac{\lambda_v^3\rho_v(\rho_l-\rho_v)g\left(h_{fg}+0.4C_{pv}\Delta T\right)}{D_o\mu_v\Delta T}\right]^{1/4} \quad \text{(Eq 28)}$$

The change from film boiling regime to transition boiling regime is characterized by minimum heat flux (q_{MHF}) point occurring at the Liedenfrost temperature (T_{LFP}). q_{MHF} is estimated by Zuber and Berenson's equation (Ref 45, 46).

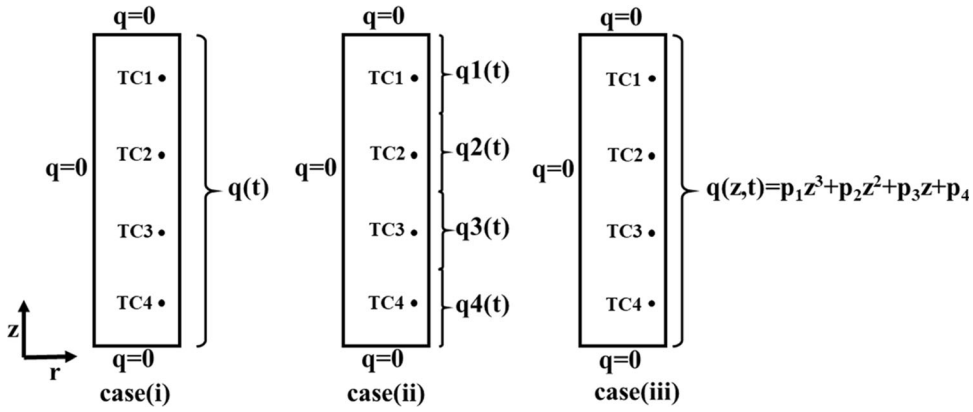

Fig. 6. Axisymmetric model of cylindrical probe used in the inverse method: case(i) single unknown heat flux boundary, case (ii) multiple unknown heat flux boundary segments, and case (iii) heat flux as a polynomial function of axial length (z) (TC1, TC2, TC3, and TC4 are locations of temperature measurements and q = 0 indicates insulated boundary)

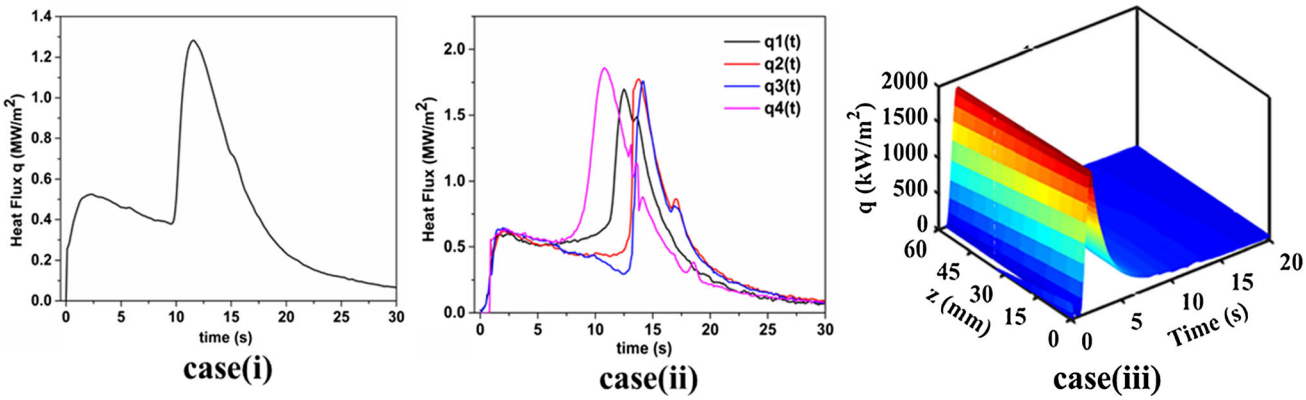

Fig. 7. Typical estimated heat flux v/s time plot obtained with various inverse models. Reprinted by permission from Springer Nature Customer Service Centre GmbH: Springer Nature, *Metallurgical and Materials Transactions A,* Effect of Bath Temperature on Cooling Performance of Molten Eutectic $NaNO_3$-KNO_3 Quench Medium for Martempering of Steels, K.M.P. Rao, K.N. Prabhu, Copyright 2017 [42]

$$q_{\mathrm{MHF}} = 0.09\rho_v h_{fg}\left[\frac{g(\rho_l-\rho_v)}{\rho_l+\rho_v}\right]^{1/2}\left[\frac{\gamma_{lv}}{g(\rho_l-\rho_v)}\right]^{1/4} \quad \text{(Eq 29)}$$

The critical heat flux (q_{CHF}) is estimated using Zuber's relation (Ref 46).

$$q_{\mathrm{CHF}} = 0.131\rho_v h_{fg}\left[\frac{\gamma_{lv}g(\rho_l-\rho_v)}{\rho_v^2}\right]^{1/4} \quad \text{(Eq 30)}$$

The effect of subcooling (cooling the specimen in a quench bath maintained at a temperature lower than the saturation temperature of the fluid) on the critical heat flux is estimated as shown below (Ref 47).

$$\frac{q_{\mathrm{CHF,subcool}}}{q_{\mathrm{CHF,sat}}} = 1 + 0.345.Ja.Pe^{-1/4} \quad \text{(Eq 31)}$$

$$Ja = \frac{\rho_l C_p \Delta T_{\mathrm{sub}}}{\rho_v h_{fg}} \quad \text{and} \quad Pe = \frac{\gamma_{lv}^{3/4}}{\alpha[g(\rho_l-\rho_v)]^{1/4}\rho_v^{1/2}} \quad \text{(Eq 32)}$$

q_{MHF} and q_{CHF} are then corrected for local variation of heat transfer with time and surface properties of the specimen as shown in Eq 32 and 33.

$$Q'_{\mathrm{MHF}} = K_{\mathrm{mhf}} Q_{\mathrm{MHF}} \quad \text{(Eq 32)}$$

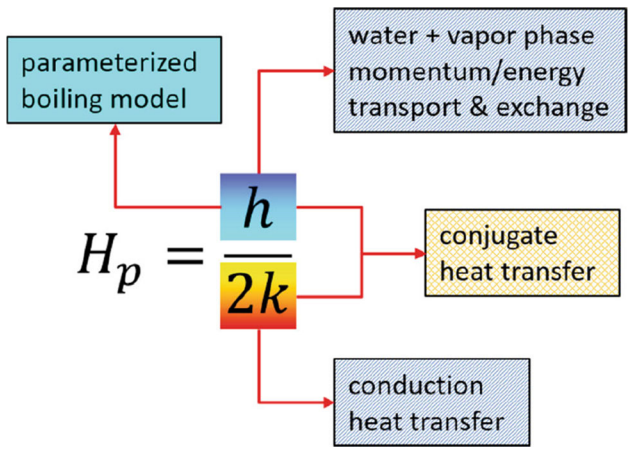

Fig. 8. Local quench severity acting on an infinitesimal area and classification of heat transfer between the metal and quenchant into four different heat transfer models. Reprinted by permission from Springer Nature Customer Service Centre GmbH: Springer Nature, *Journal of Materials Engineering and Performance,* On the Development of Parametrical Water Quenching Heat Transfer Model Using Cooling Curves by ASTM D6200 Quenchometer, J. Jan, D. S. MacKenzie, Copyright 2020 [43]

$$Q'_{\mathrm{CHF}} = K_{\mathrm{chf}} Q_{\mathrm{CHF}} \quad \text{(Eq 33)}$$

K_{mhf} and K_{chf} are application-specific factors. In addition to it, another application-specific factor known as dry phase pack limit (α_{DPPL}), which gives the maximum volume fraction of vapor phase is calculated. The parameters K_{mhf}, K_{chf}, T_{LFP} and α_{DPPL} are calibrated by performing the quenching experiment, after which the boiling heat transfer model is applied to model the quenching process. The authors have used the cooling curve analysis method based on the ASTMD6200/ISO9950 standard (quenchometer) to calibrate the boiling heat transfer model. The cooling curves obtained by the experiment were parameterized based on the CHF, minima, and maxima of the second derivative of the temperature v/s time data for the reconstruction of cooling curves. The simulated and measured data were optimized by the use of a parameter known as the cost function. The cost function provides a correlation between simulated and measured data. The smaller the cost function value, the closer the predicted data is to the experimental results.

Vorster et al. (Ref 48) modeled the residual strain distribution while quenching a 316L stainless steel cylinder in a water bath. The thermal boundary condition was modeled using the empirical boiling heat transfer correlations. The different cooling regimes during cooling, i.e., film boiling, transition boiling, nucleate boiling, were modeled using the boiling heat transfer correlations. The thermal boundary conditions calculated from the empirical equations for various degree of subcooling (ΔT_{sub}) are shown in Fig. 9. The elastic residual strain distribution was modeled using the FE simulation. Experimental measurements of residual stress by neutron diffraction was used to validate the simulation. Figure 10(a) shows the simulated and measured residual strain distribution. It was observed that the accurate representation of the thermal boundary condition improved the accuracy of the prediction of residual strains. Although the increase in subcooling had a comparable critical heat flux (CHF), the path traced by the transition boiling differed significantly. The increase in subcooling showed a rise in rewetting temperature (Liedenfrost) and the length of transition boiling stage. The effect of subcooling on the residual strain distribution showed that the increase in subcooling increased the residual elastic strain. The region of strain field was observed to extend toward the center of the specimen, as shown in Fig. 10(b). Therefore, the variation of transition boiling stage or the path traced by the rewetting phenomena significantly affects the final residual stress distribution in the quenched specimen.

Juarez et al. (Ref 49) investigated the sensitivity of surface heat transfer coefficient (HTC) on the accuracy of prediction of residual stresses in quenched 304L stainless steel Jominy end quench specimen. The specimen dimension was ϕ25 mm × 100 mm. The heated specimen was cooled by a water jet at the bottom end. The heat transfer coefficient at the quenched end was estimated using the inverse method. The heat transfer coefficient (HTC) was varied by providing ± 10 KW/m^2 HTC shifts, ± 100°C temperature shifts, and combined HTC and temperature shifts. The predicted residual stresses were validated by experimental measurement by the contour method. It was observed that the FE model overestimated maximum tensile residual stress by about 20%, and the compressive residual stress maxima were underestimated. However, the position of occurrence of maxima was accurately predicted. Furthermore, no significant influence on residual stress distribution was shown by the variance of HTC and temperature shifts. Nevertheless, the negative HTC and temperature shifts and their combination reduced the magnitude of tensile residual stress and shifted its maxima position toward the quenched end. The compressive residual stress remained unchanged with variation in HTC. Since no phase transformation is involved, the overestimation of tensile residual stress was attributed to the plasticity effect due to the twinning of austenite grains during quenching.

The boiling heat transfer correlation for predicting temperature distribution requires the thermophysical properties of the quenchant in both liquid and vapor phases and their latent heat. In the case of standard liquids such as water, these properties are readily available. These properties are to be measured for quenchants such as oil, aqueous polymer, nanofluids, and molten salts. In addition, the heat transfer with oil and polymer media includes a certain level of decomposition of quenchant near the metal/quenchant interface. With nanofluids, the nanoparticles suspended in the liquid show a different heat transfer mechanism.

Furthermore, the nanoparticles adhere to the heated metal surface, causing premature destabilization of vapor film. Therefore, boiling heat transfer correlations for modeling the thermal boundary condition would not be suitable in such cases. On the other hand, the inverse heat conduction method is a more convenient method for estimating the boundary heat transfer coefficient as the estimation is based on the thermal history inside the specimen and is therefore impervious to the changes occurring at the metal/quenchant interface.

7. Application of Artificial Neural Network Model for Prediction of Residual Stress

Machine learning algorithms such as the artificial neural network (ANN) are used to simulate highly nonlinear systems that cannot be solved with a simple regression model. The neural network is an interconnection of small units known as perceptron (the equivalent of biological neurons). The most common neural network architecture is the feed-forward network consisting of the input, hidden, and output layers. Initially, the training of neural networks is done with a set of known input/output data. Training estimates the synaptic weights corresponding to each neuron such that the global error of prediction is minimized (Ref 50). Finally, the validation is done with a set of test data. In quenching, the ANN model is applied in combination with the FE simulation. The predicted output from the FE quenching simulation is used to train and validate the ANN model.

Bouissa et al. (Ref 51) used 3D FE simulation with ANN to predict the boundary heat transfer coefficient while quenching a large steel forged block. The ANN model was trained using the output of the FE simulation. The calculated cooling curves within the forged block were input. The ANN architecture was a feed-forward network with a single hidden layer. The mean absolute prediction error by the ANN was less than 1.47%. Toparli et al. (Ref 52) investigated the ANN prediction

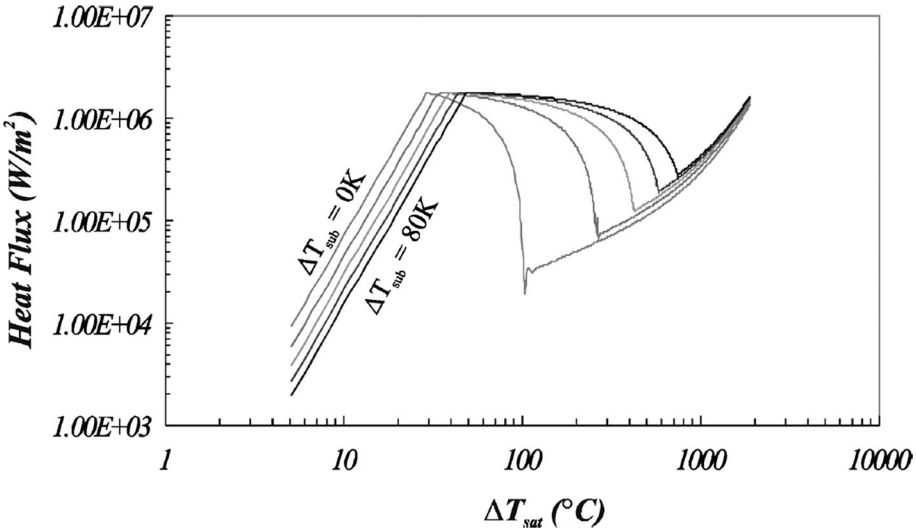

Fig. 9. Thermal boundary conditions estimated using empirical heat transfer correlations. From Influence of Quenchant Hydrodynamics and Boiling Phase Incipient Temperature Shifts on Residual Stress Formation, W. J. J. Vorster, M. W. Van Der Watt, A. M. Venter, E. C. Oliver, D. G. L. Prakash, A. M. Korsunsky, *Heat Transfer Engineering,* 2009, reprinted by permission of the publisher (Taylor & Francis Ltd, http://www.tandfonline.com) [48]

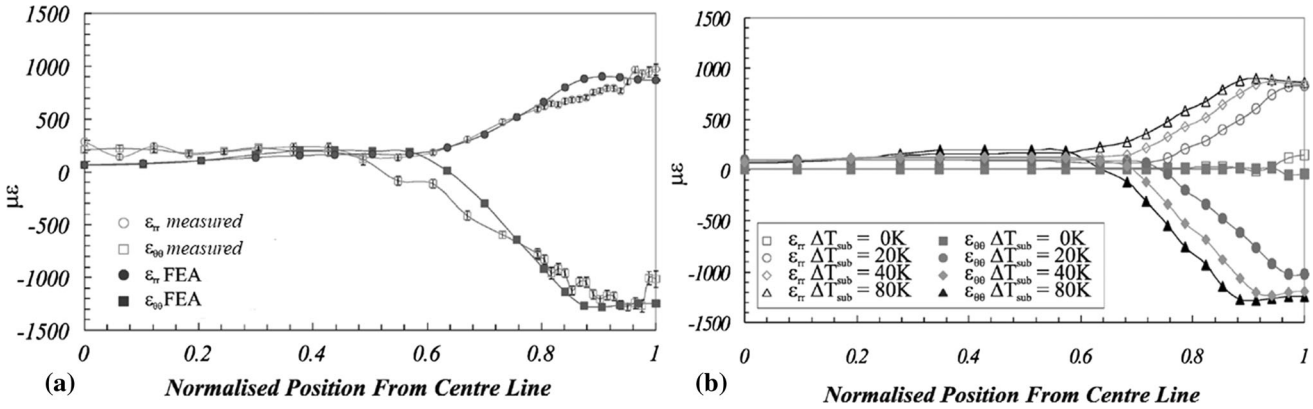

Fig. 10. (a) Residual strain distribution (b) effect of subcooling on residual strain distribution (ε_{rr} -radial residual strain and $\varepsilon_{\theta\theta}$-tangential residual strain). From Influence of Quenchant Hydrodynamics and Boiling Phase Incipient Temperature Shifts on Residual Stress Formation, W. J. J. Vorster, M. W. Van Der Watt, A. M. Venter, E. C. Oliver, D. G. L. Prakash, A. M. Korsunsky, *Heat Transfer Engineering,* 2009, reprinted by permission of the publisher (Taylor & Francis Ltd, http://www.tandfonline.com) [48]

efficiency of cooling curves and longitudinal thermal residual stress in AISI 1020 steel cylinders of various diameters quenched in water from 600 °C. The ANN was feed-forward with three hidden layers. The diameter, height of the cylinder, and cooling time were the input to the model. The output predicted the cooling curves at the surface and the center. A similar ANN was used to predict longitudinal residual stress where the output layer consisted of residual stresses at the center and surface. The FE quenching simulation output was used to train and validate the ANN. The predicted ANN output precisely matched the FE output. In addition, the computation time was drastically reduced. The simulation completion took 2 h in the FE process, whereas the ANN took only 15 minutes in an 800Hz processing speed computer.

Similar ANN models in conjunction with FE simulation have been used by Hanza et al. (Ref 53) and Rao and Prabhu (Ref 54) for predicting hardness during the heat treatment process. The ANN algorithm has shown excellent prediction accuracy.

8. Factors Affecting Residual Stress during Quenching

8.1 Effect of Specimen Geometry and Section Thickness on the Residual Stress

The difference in the cooling rates across the specimen during quenching cause substantial temperature difference that lead to a thermal gradient. If the thermal gradient is large, unequal contraction and the differential cooling between the surface and the core of the specimen cause the unequal thermal and transformation stress distribution in the specimen. For a thin specimen such as sheet metals, the quenching stresses are enough to distort or warp. For the specimen with a large section thickness, the bending and warping forces are resisted by its geometrical configuration. Thus, high residual stresses are induced in the specimen, leading to dimensional instability during the component's service life (Ref 9, 55).

The quench specimen parameters such as size, geometry, and material properties significantly affect the heat transfer rate from the specimen surface during quenching and, in turn, affect the temperature distribution, residual stress and distortion of the component. Ramesh and Prabhu (Ref 56) investigated the effect of the quench component size, geometry (plate, cylinder, and sphere), and material type (Silver, Copper, Nickel 200, Stainless-Steel and Inconel 600) in combination with the boundary heat transfer coefficient on the mean cooling rate of the component. It was observed that the size of the component and the material property majorly affected the mean cooling rate. Furthermore, a dimensionless cooling parameter L^2CR/α was defined (L—characteristic length, CR-mean cooling rate, α—thermal diffusivity). The cooling parameter was found to vary exponentially with the Biot number (hL/λ) as shown below.

$$\frac{L^2CR}{\alpha} = a + be^{-cBi} \quad \text{(Eq 34)}$$

a, b and c are the regression constants, and Bi is the Biot number. The experiment showed that for Biot number greater than 0.8, the component's geometry was the dominant parameter controlling the mean cooling rate. The section thickness of the specimen influences the heat transfer during quenching. The effect is visualized by the change in heat flux magnitude at the metal/quenchant interface. Nayak and Prabhu (Ref 57, 58) investigated the effect of section thickness on the metal/quenchant interfacial heat flux by quenching 304 stainless steel and plain carbon steel probes (AISI 1045 and 1090) of 25 and 50 mm diameter while quenching in vegetable oils and mineral oil. The estimated heat flux indicated that the increase in the section thickness increased the maximum heat flux value. A similar observation was found by Babu (Ref 59), where quenching was performed with a stainless-steel probe of varying diameters in water. Ramesh and Prabhu (Ref 60) investigated the effect of surface heat transfer coefficient on the average cooling rate of the stainless-steel quench probe of various section thicknesses. It was observed that for small diameter probes, the mean cooling rate at the center of the probe varied linearly with the heat transfer coefficient. However, for higher diameter probes, the variation was exponential. The authors further suggested a critical diameter above which the effect of section thickness on cooling rate becomes negligible for any boundary heat transfer coefficient. An empirical model (Eq 35) was proposed correlating the mean cooling rate (CR) of the quench probe with the diameter (D) of probe and severity of cooling media, which is quantified by the Grossmann number (H).

$$D^2\mathrm{CR} = \frac{2H\lambda D}{1625.06 + 47.1874H\lambda D - 46.2037\sqrt{H\lambda D}} \quad \text{(Eq 35)}$$

λ in Eq 35 refers to the thermal conductivity of the quench probe.

Gur (Ref 61) investigated the effect of the specimen's geometry on the residual stress formation through the X-ray diffraction technique. Steel cylinders having varying hole diameters and eccentricity ratios were used in the study. Changing the eccentricity ratio provided a continuous change in the thickness along the circumference of the specimen. It was observed that the surface tangential residual stress changed sign from compressive to tensile as the hole diameter increased. Eccentricity resulted in a complex pattern of residual stress distribution along the circumference of the specimen. The thin section often showed tensile residual stress, and the thick section showed compressive stress. Increasing the hole diameter increased the magnitude of residual stress and even resulted in cracking. The effect of eccentricity was decreased with the increase of hole diameter. The result holds good for steels of low hardenability. The effect of hole diameter and eccentricity was not pronounced with higher hardenability steels as they produced more or less uniform microstructure throughout the specimen. Simsir and Gur (Ref 62) further analyzed the effect of hole diameter and eccentricity on the residual stress distribution using the 3D finite element (FE) simulation. The results indicated that the quenching model could efficiently predict the residual stress distribution in an asymmetric geometry. The changes in residual stress distribution were susceptible to the small changes in eccentricity and hole diameter.

8.2 Cooling Uniformity

In the quenching process, the uniformity of heat removal from the surface of the specimen plays a significant role in minimizing residual stress and distortion of the specimen. Nonuniform cooling is one of the main reasons for distortion and cracking. Nonuniformity in cooling during quenching arise due to the rewetting phenomena occurring at the metal/quenchant interface. Ramesh and Prabhu (Ref 63) studied the axial and radial variation in temperature distribution while quenching a simple cylindrical probe in mineral oil. The temperature measurements were made at various axial and radial locations of the probe with the help of thermocouples. The inverse heat conduction method estimated the spatially varying transient surface heat flux. The axial variation in the heat flux was observed to be about 171 kW/m^2 in the vapor blanket stage and 498 kW/m^2 in the nucleate boiling stage. In the radial direction, the variation in the surface heat flux was 35 and 195 kW/m^2, respectively. The significant heat flux variation was attributed to the nonuniformity caused by the motion of the wetting front and its irregular geometry. Figure 11 shows the uneven temperature distribution in axial and radial directions of the Inconel 600 probe while quenching in mineral oil.

Figure 12(a) and (c) shows the variation of wetting front velocity and rewetting temperature along the probe length while quenching a cylindrical metallic probe in brine and polymer quenchants, respectively. Figure 12(b) and (d) shows the corresponding effect of wetting front movement on the peak heat transfer coefficients (HTC) and HTCs at 705, 550, 300, and 200 °C for brine and polymer quenching, respectively. It is observed that the magnitude of HTC depends on the magnitude of wetting front velocity. Higher wetting front velocity yields higher HTC values. The spatial variation of wetting front velocity and rewetting temperature depends on the mode of heat transfer taking place at the metal/quenchant interface. Brine quenchant showed a random nature of rewetting and hence nonuniform wetting front motion, whereas with the polymer quenchant, the wetting initially occurred with the collapse of the polymer film and subsequently the movement of the wetting front from the bottom to the top of quench probe. The more vigorous cooling in brine increased the magnitude of HTC, but the spatial uniformity of HTC was less compared to that with the polymer quenchant. The wetting front/rewetting velocity was measured by video recording the quenching process and the estimated interfacial heat flux versus time plots at various axial locations (Ref 64).

Figure 13 shows the dependency of the magnitude of metal/quenchant interfacial heat flux on the wetting front (rewetting) velocity. The wetting front velocity measurement and the heat flux estimation are performed for an Inconel 600 cylindrical standard quench probe (ISO 9950). Since the Inconel 600 does not undergo phase transformation, the estimated heat flux could be used to compare the cooling performance of various quenchants. In the figure, the pattern shows an increasing trend of heat flux with increased wetting front velocity. Figure 14 shows the effect of wetting front velocity on the spatial variation of heat flux along the axial direction. It is observed that the variation of heat flux depends not only on the wetting front velocity but also on the type of quenchant used.

The vegetable oils and pure PAG (polyalkylene glycol) grouped into cluster 6 displayed wetting front velocities in the range of 2.5-20 mm/s and showed the lowest spatial variation of heat flux (50-150 kw/m^2). Although the mineral oils, martempering oils, and 75% PAG in water showed lower wetting front velocity (5-10 mm/s), the spatial variation of heat flux was higher than vegetable oils (150-250 kW/m^2). Clusters 1, 2, and 5 consist of water, water-based nanofluids, and aqueous polymer solutions. The wetting front velocity for these groups of quenchants is spread over a broader range and showed a higher spatial variation of heat flux. Brine quenchant with the highest wetting front velocity (44.85 mm/s) showed the maximum spatial variation of heat flux (646 kw/m^2). Higher heat flux variation with water-based nanofluids, aqueous polymer and brine could be attributed to different heat transfer mechanisms than conventional oil quenchants. In nanofluids, the nanoparticles form a colloidal solution with the base fluid. The mechanisms such as the Brownian motion, liquid layering, phonon transport, and the clustering of nanoparticles differ the heat transfer mechanism from that of conventional liquids (Ref 73). In addition, the deposition of nanoparticles on the metal surface while quenching in nanofluids could create a higher spatial variation of heat flux (Ref 74). In the case of PAG polymer solution and brine, explosive type of wetting is observed, leading to a substantial increase in wetting front velocities and the spatial variation of heat flux (Ref 64). Figure 15 shows the effect of wetting front velocity on the Leidenfrost or the minimum film boiling temperature. An increase in Leidenfrost temperature usually indicates a shorter film boiling duration. The mineral oils showed the lowest Leidenfrost temperature, followed by vegetable oils, martempering mineral oils, and water-based nanofluids. Water and aqueous polymer solution showed the highest Leidenfrost temperatures.

Figure 16 shows the effect of rewetting time on the spatial variation of heat flux in the circumferential direction. The variation of heat flux along the circumferential direction is mainly due to the geometry of the wetting front. The irregularities in the geometry of the wetting front could be

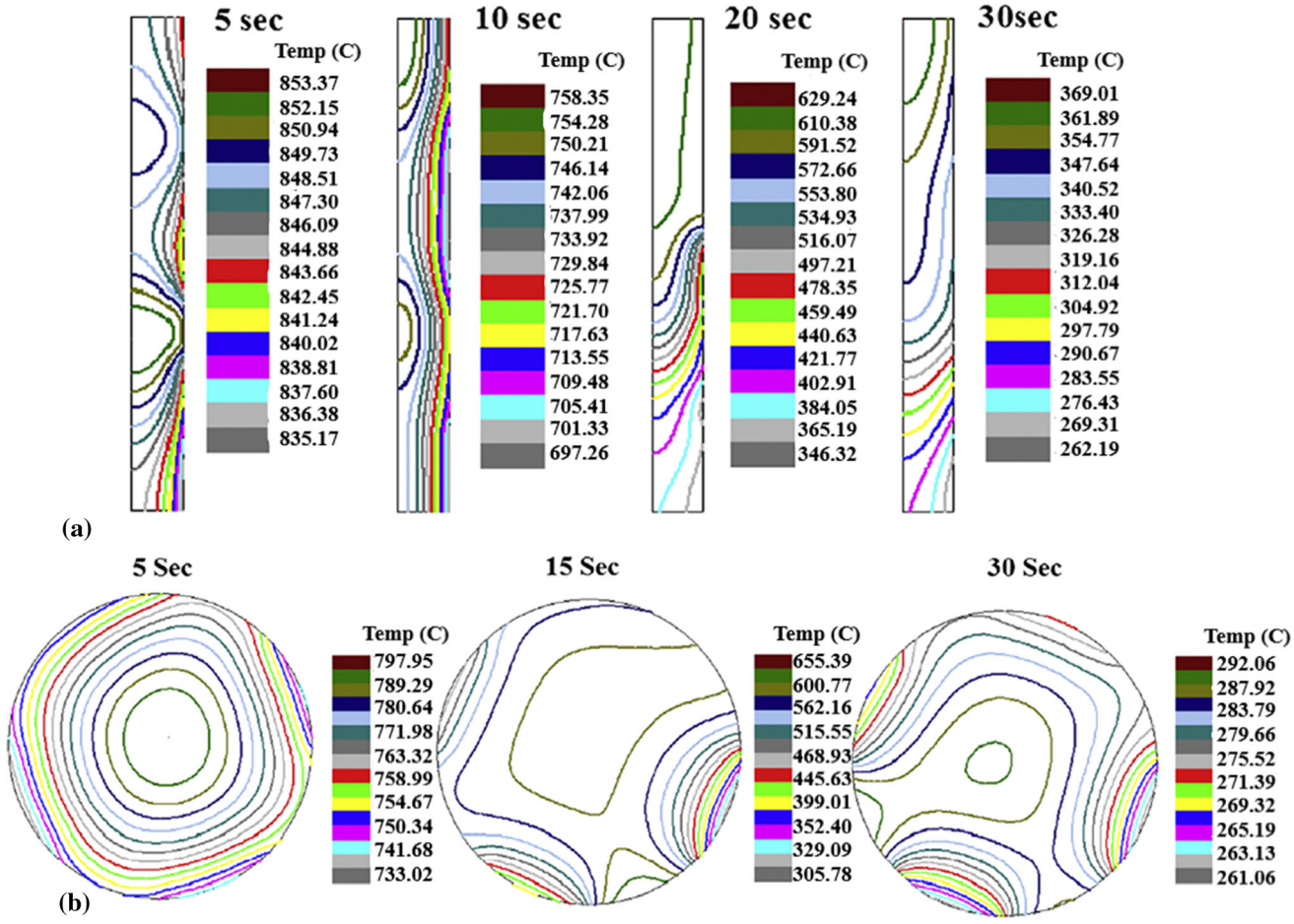

Fig. 11. Temperature distribution in the cylindrical quench probe while quenching in mineral oil, (a) axial temperature variation and (b) radial temperature variation. Reprinted from *Experimental Thermal and Fluid Science,* Vol 54, G. Ramesh, K. N. Prabhu, Assessment of Axial and Radial Heat Transfer During Immersion Quenching of Inconel Probe, pages 158-170, Copyright 2014, with permission from Elsevier [63]

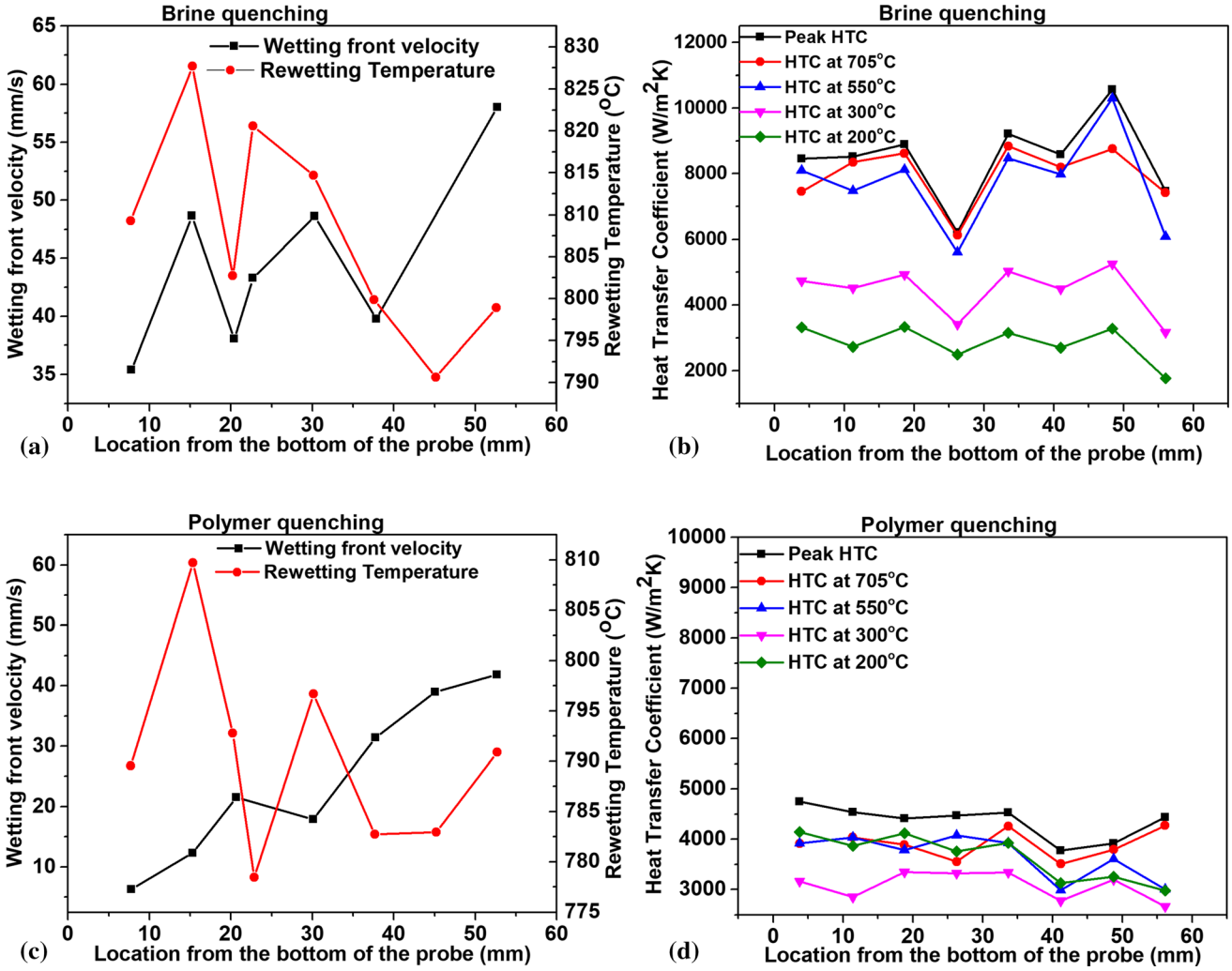

Fig. 12. Spatial variation of wetting front velocity, rewetting temperature and heat transfer coefficients along the axial length of the ISO 9950 cylindrical probe for brine and polymer quench media. Reprinted by permission from Springer Nature Customer Service Centre GmbH: Springer Nature, *Metallurgical and Materials Transactions B,* Spatial Dependence of Heat Flux Transients and Wetting Behavior During Immersion Quenching of Inconel 600 Probe in Brine and Polymer Media, G. Ramesh, K.N. Prabhu, Copyright 2014 [64]

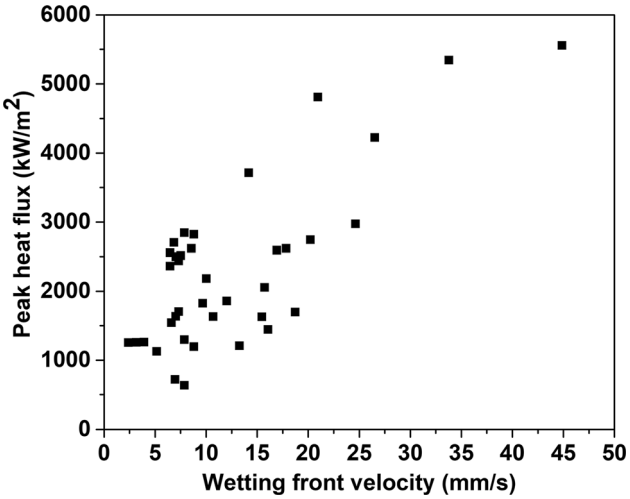

Fig. 13. Effect of wetting front velocity on the magnitude of the peak heat flux [38, 64-72]

quantified by measuring the difference in the rewetting time along the circumferential direction. Oil quenchants (vegetable and martempering mineral oils) and high concentration aqueous polymer solutions showed the lowest heat flux variation along the circumferential direction. Water, low concentration PAG (5, 10 and 25%) in water and brine showed the highest circumferential variation due to explosive type of wetting. Conventional mineral oils, fast mineral oils, 50% PAG/water, and 4% PVP polymer solution showed a moderate heat flux variation in the circumferential direction. The data for Fig. 13, 14, 15 and 16 are obtained from references (Ref 38, 64-72)

Rao and Prabhu (Ref 75-77) studied the nonuniformity in heat transfer while quenching an Inconel 600 quench probe with neem oil at higher bath temperatures, hot oil (martempering mineral oil), binary and ternary molten salt bath ($NaNO_3$-KNO_3 and KNO_3-$NaNO_3$-$NaNO_2$) quench media. The uniformity of heat extraction was quantified by a parameter E_Z, defined as the normalized energy extracted along the length of the probe (z). E_Z was calculated as shown in Eq 36. Figure 17(a)

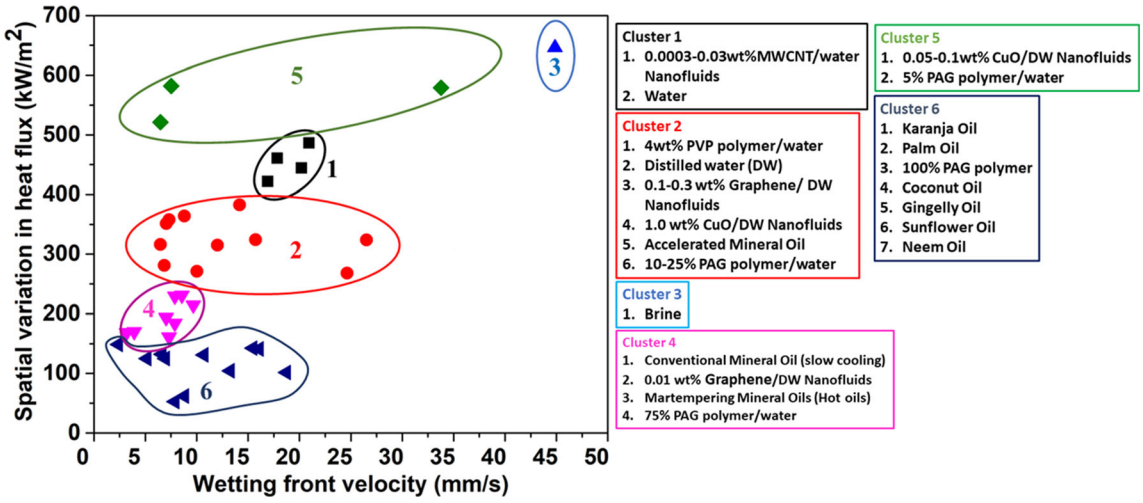

Fig. 14. Variation of heat flux along the axial direction with the increase in wetting front velocity [38, 64-72]

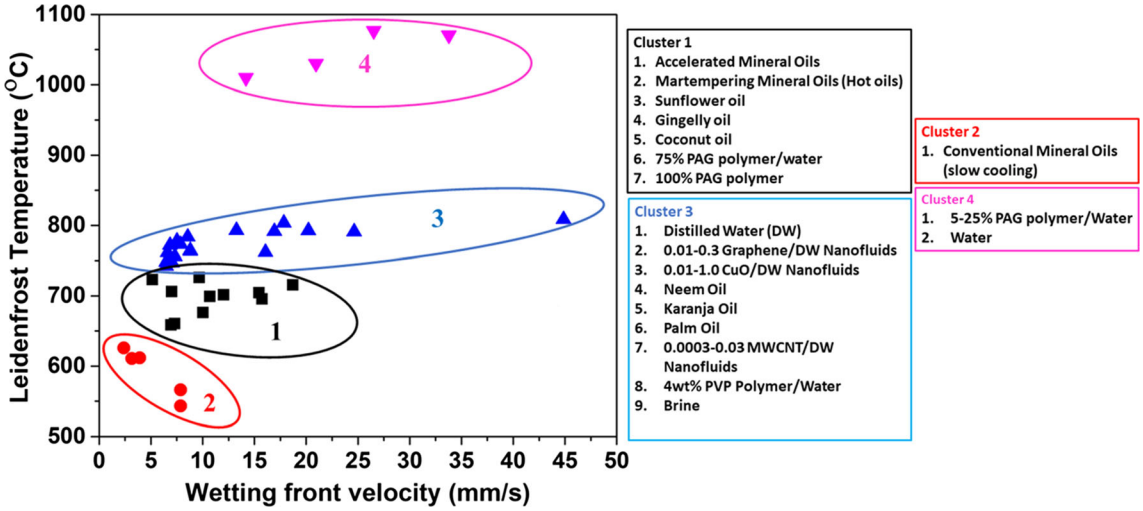

Fig. 15. Effect of wetting front velocity on rewetting/Leidenfrost temperature [38, 64-72]

and (b) shows the variation of energy extracted from the surface along the length of the probe for hot oil and neem oil, respectively. Figure 17(c) shows the variation of normalized energy extracted along the length of the quench probe for molten salt baths. A more significant variation of E_Z along the probe length indicates nonuniform heat transfer.

$$E_Z = \frac{\int_0^t q(t,z)\mathrm{d}t}{\max\left(\int_0^t q(t,z)\mathrm{d}t\right)} \quad \text{(Eq 36)}$$

where $q(t,z)$ is the spatial and temporally varying heat flux.

Racking arrangement, rate of immersion, and agitation are the other factors affecting the uniformity of heat transfer during quenching. Racking is essential when quenching has to be performed in batches. The specimens are positioned inside the furnace with the help of a rack, clamps, wires, steel baskets, and other fixtures. The racks, clamps, or fixtures should be neither too tight to accommodate the thermal expansion during heating of the specimen nor too loose to avoid sagging of part. The specimens should not be spaced too closely. Due to thermal expansion during heating, specimens will come in contact with each other, and as a result, contact pressure develops. The specimen will resort to warpage or distortion to relieve the contact pressure and conform to the confined space (Ref 8). Garcia et al. (Ref 78) investigated the effect of immersion rate on the microstructure, hardness, residual stress, and distortion of SAE 5160 rectangular steel plates. Immersion rates of 10, 20, 60,100 and 140 mm/s were used. It was observed that the immersion rates above 60mm/s showed a higher volume fraction of martensite, higher hardness, lower residual stress, and distortion. The effect of immersion rates on the residual stress and distortion of the samples was significant. Increasing immersion rates showed a decreasing trend of residual stress and distortion.

Agitation of quench medium helps in early and uniform rupture of the vapor blanket stage and thereby improves uniformity of cooling. The agitation rate has to be maintained optimum. Low agitation rate has minimal effect on elimination of vapor blanket stage whereas, excessive agitation causes strong turbulence across the specimen surface. The material being soft at a higher temperature may distort due to higher fluid pressure (Ref 9, 58). Sedighi and McMohan (Ref 79) investigated the effect of quenchant (oil) flow speed and part orientation on the heat transfer coefficient and subsequent

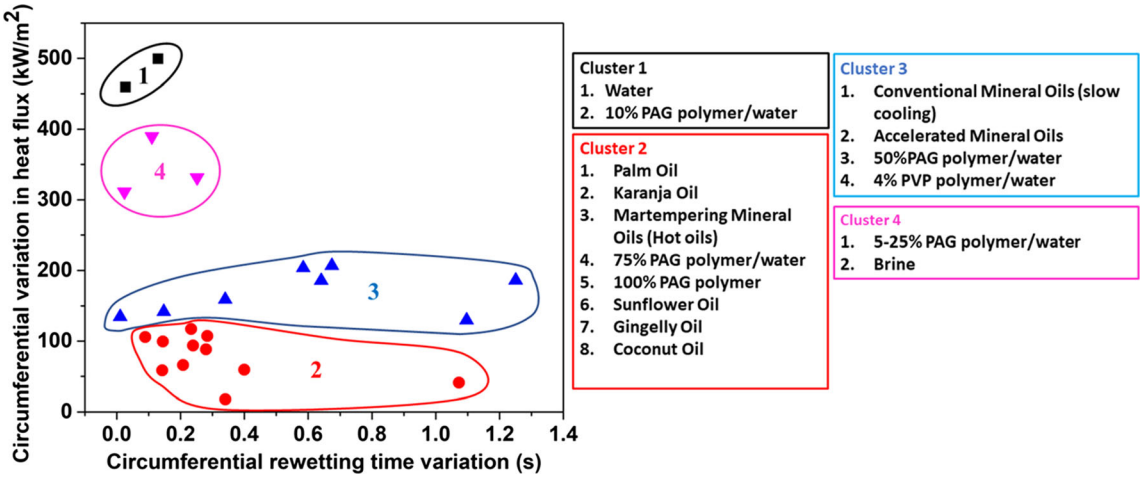

Fig. 16. Effect of rewetting time on the spatial variation of heat flux in the circumferential direction [38, 64-72]

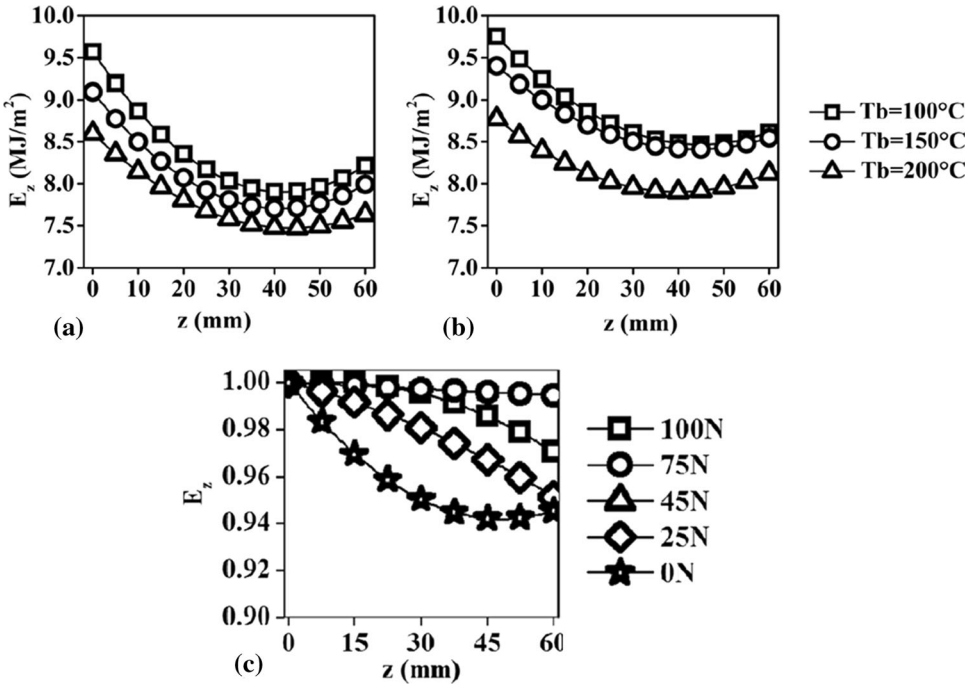

Fig. 17. Variation of Ez along the quench probe length quenched in (a) hot oil, (b) neem oil at various bath temperatures and (c) normalized Ez for KNO_3-$NaNO_3$ molten salt baths of various compositions. Reprinted by permission from Springer Nature Customer Service Centre GmbH: Springer Nature, Journal of Materials Engineering and Performance, Assessment of Cooling Performance of Neem Oil for Distortion Control in Heat Treatment of Steel, K. M. P. Rao, K. N. Prabhu, Copyright 2020 *and* Springer Nature, Journal of Materials Engineering and Performance, Compositional and Bath Temperature Effects on Heat Transfer During Quenching in Molten $NaNO_3$-KNO_3 Salt Mixtures, K. M. P. Rao, K. N. Prabhu, Copyright 2020 [75-77]

residual stress development in the material. The study showed that the careful control of oil speed combined with proper part orientation could help achieve uniformity in residual stress distribution.

8.3 Quenchant Selection

Nunes et al. (Ref 80) investigated the effect of austenitizing temperature, time, and type of quenchant (oil and water) on the hardness and distortion of AISI 4340 steel using ANOVA analysis. A distortion study was performed using the Navy C-ring specimen. The result indicated that the type of quenchant had a significant effect on the hardness and distortion of the specimen. Therefore, an appropriate quenchant with a suitable combination of parameters has to be selected to minimize the distortion. The quenchant under consideration should meet the following criteria (Ref 8): (1) The cooling rate offered by the quenchant should be high enough to surpass the critical cooling rates for the metal or alloy being quenched for achieving desirable mechanical properties. (2) The cooling rate must be slow enough in the martensitic transformation range to minimize distortion in the quenched component. Therefore, for selecting the quenchant, two critical parameters need to be known. (1) The quench sensitivity or hardenability of the alloy

to assess the required severity of quench medium and (2) the cooling characteristics of quenchant at various temperature ranges. The Grossman H value substantiates the quench severity. The H value typically ranges from 0.1 (for oil medium with no agitation) to 5.0 (brine solution) or more (High-pressure fluid). Low hardenability steels require a quench medium with high quench severity. Quenching optimal and higher hardenability steels with a high quench severity medium will increase the propensity of distortion and cracking due to high thermal stress (Ref 9). The cooling characteristics of the quenchant depend on its thermophysical properties (Ref 81). The heat transfer characteristics of a quench medium are assessed by cooling curve analysis according to ASTM D6200 and ISO 9950 standards with a standard probe made of Inconel 600 alloy (Ref 82). Prabhu and Ramesh (Ref 83) proposed a quantitative model for predicting the cooling rate of the Inconel 600 quench probe while quenching in various quench mediums. By knowing the thermophysical properties of quench medium such as the thermal conductivity (k), kinematic viscosity (υ), surface tension (γ_{lv}), and equilibrium contact angle or wetting angle (θ) the mean cooling rate could be estimated. The mean cooling rate between 730 and 260 °C ($CR_{730\text{-}260}$) of the probe was correlated with the thermophysical properties of the quench medium as shown below.

$$CR_{730-260} = \frac{\chi}{2259.27 + 0.007\chi + 4.15\sqrt{\chi}} \quad \text{(Eq 37)}$$

where $\chi = \frac{k}{\upsilon\gamma_{lv}\cos\theta}$

The equation provided a good prediction of cooling rate for χ in the range of 6667-2.44 $\times$ 10^8 m^{-1} K^{-1}.

Figure 18 shows the effect of fluid flow properties such as kinematic viscosity and solid–liquid interfacial tension of the quench media on the wetting front velocity. The solid–liquid interfacial tension (γ_{sl}) is calculated from the Young–Dupre equation given by:

$$\gamma_{sl} = \gamma_{sv} - \gamma_{lv}\cos\theta_e \quad \text{(Eq 38)}$$

γ_{sv} and γ_{lv} are surface energy of the solid substrate and the surface tension of the liquid, respectively. θ_e is the equilibrium contact angle. Since γ_{sv} is substrate dependent, the term $\gamma_{lv}\cos\theta_e$ gives an approximation of solid/liquid interfacial tension for various quenchants.

It can be observed from Fig. 18 that the wetting front velocity decreases steeply with the increase in viscosity. The viscosities in the range of 0.5-2 mm^2/s (thin fluids) have shown high wetting front velocities (20-45 mm/s). Thicker fluids such as oils and high concentration polymer solutions have lower wetting front velocity ($<$ 20 mm/s). $\gamma_{lv}\cos\theta_e$ also shows a decreasing trend of wetting front velocity. As $\gamma_{lv}\cos\theta_e$ increases, γ_{sl} decreases, causing an extended film boiling stage and, as a result, lower wetting front velocity leading to nonuniform heat transfer and decrease in the magnitude of heat flux (Ref 38).

Figure 19 shows the effect of thermal conductivity, kinematic viscosity, and the solid/liquid interfacial tension on the magnitude of peak heat flux.

The average value of peak heat flux decreased with an increase in viscosity and $\gamma_{lv}\cos\theta_e$, whereas it increased with the increase in the thermal conductivity of the fluid. The trend of average peak heat flux roughly shows an exponential decrease with viscosity and linear behavior with thermal conductivity and $\gamma_{lv}\cos\theta_e$, respectively. The contact angle (θ_e) indicates the degree of wettability of the quench medium on the surface of the quenched sample. Typically, a lower contact angle (less than 90°) indicates good wettability. As θ_e decreases, the value of cos θ_e approaches unity, and as a result, the value of $\gamma_{lv}\cos\theta_e$ increases. The increase in $\gamma_{lv}\cos\theta_e$ decreases the value of solid/liquid interfacial tension. Thus, it could be inferred that a very low contact angle (say $<$ 20°) stabilizes the vapor film leading to lower rewetting velocity, decreased peak heat flux value, and an increase in nonuniformity of heat transfer. The wettability is not solely a quenchant property but also depends on the surface roughness of the quenched sample. For oil quenchants (high viscosity), the lower surface roughness of the sample increases the wettability and heat transfer rate, whereas, for water or brine (low viscosity), a higher value of surface roughness shows increase in wettability and heat transfer rate (Ref 84). The data for Fig. 18 and 19 were obtained from the references (Ref 38, 64-72). Table 2 shows the thermophysical properties of various quenchants, the rewetting velocity, and the magnitude of peak heat flux obtained while quenching with the cylindrical Inconel 600 standard probe.

Table 3 compares the viscosity of quenchants, the heat transfer coefficient (HTC), and residual stress developed after quenching. For oil quenchants, it is observed that very high viscosity (ESBO) and very low viscosity (FAME) decrease HTC and increase the magnitude of residual stress. The viscosity of oils roughly in the range of (20-60 cSt) has shown residual stress in the range of 100-300 MPa without any significant reduction in HTC. The higher viscosity of oil quenchants is usually associated with higher boiling temperature, and therefore the film boiling stage is minimal or absent (Ref 85). The increase in the residual stress in high-viscosity quenchants could be attributed to insufficient fluid circulation in the vicinity of the heated specimen, whereas in the low-viscosity quenchants, nonuniformity of heat transfer due to rewetting phenomena is the predominant cause for the increase in residual stresses.

The concerns related to global warming and environmental pollution with mineral oil quenchants have led to a search for alternative eco-friendly quenchants that are biodegradable. Vegetable oils, nanofluids, molten salts, and aqueous polymer quenchants have been developed in this context. However, the heat transfer aspects of these quenchants and the corresponding effect on hardness have been extensively discussed. The effect of quench media on residual stress formation has not been well explored. More work needs to be done in this area to arrive at a general understanding of the effect of quenchant on the residual stress evolution, which would undoubtedly help the heat-treaters select appropriate quenchants.

9. Distortion and Quench Defects

The navy C-ring test is the standard method used to analyze the quenchant effect on a steel grade distortion. The C-ring consists of a gap opening and a continuously varying thickness along the circumferential direction in the shape of the alphabet C. The gap widening or contraction after quenching is used to compare the percentage distortion associated with various quenchants. Table 4 shows the percentage distortion measured through the Navy C-ring test with various quenchants.

The distortion of the material leads to the formation of quench cracks during quenching. Both the material properties

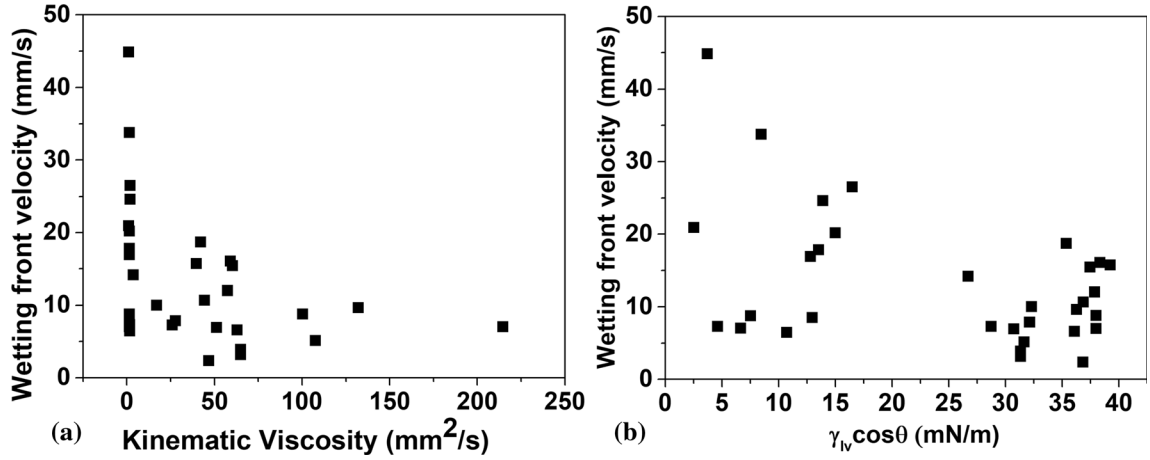

Fig. 18. Effect of (a) Kinematic viscosity and (b) Solid/liquid interfacial tension of the quenchant on the wetting front velocity [38, 64-72]

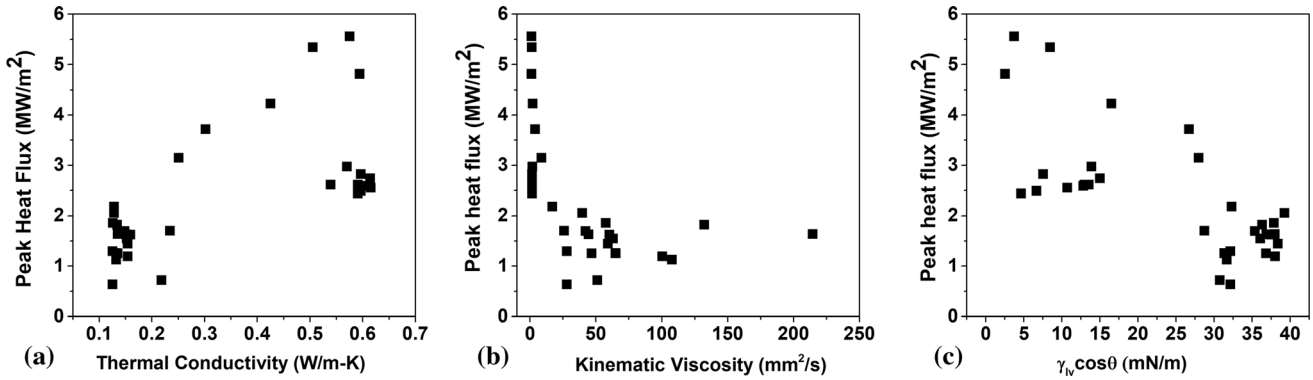

Fig. 19. Effect of (a) thermal conductivity, (b) kinematic viscosity, and (c) solid/liquid interfacial tension on the magnitude of heat flux transient during quenching [38, 64-72]

and the heat-treating conditions affect the formation of quench cracks. The properties include geometry, chemical composition, and surface conditions. The process conditions consist of nonuniform heating, wrong choice of austenitizing temperature, overheating, burning, and incorrect quenching (Ref 93). The quenchant properties that affect quench cracking are the quench severity and quench uniformity.

Quench cracks occurs due to the nonuniform heat transfer on the surface as well as within the component. On the surface, nonuniform cooling leads to differential contraction. The delayed contraction on the gradual cooling region causes pull stress, leading to pull cracking. On the other hand, nonuniform cooling within the component causes push stress. The outer region cooling first undergoes contraction, causing tensile stress in the region. The interior region is slowly cooled and undergoes compression. The compressive or push stress on the interior region causes a push crack on the fast-cooled exterior surface. Pull cracking is mainly due to nonuniform cooling from austenitizing temperature to the martensite start temperature, whereas push cracking is due to the nonuniform cooling in the martensite transformation temperature range. However, cracking in both cases occur between M_S and M_f temperature range. Quench cracking is primarily facilitated by stress raisers such as sharp edges, rapid change in the area, notches, segregation of impurities, carbides, and inclusions (Ref 94).

Figure 20 shows the quench crack propagation in the intergranular region of austenite grain boundaries due to sulfide segregation at the grain boundaries. The crack propagated due to the improper selection of austenitization temperature (Ref 93). Figure 21 shows the quench crack propagation along the surface of a cylindrical AISI 52100 steel probe quenched in distilled water and carbonated water quenchants. The presence of a hole drilled near the specimen's surface for inserting a thermocouple for measuring temperatures might have acted as a stress raiser and aided the crack propagation during quenching (Ref 95).

10. Minimizing Residual Stresses and Distortion during Quenching

The residual stresses in a material due to quenching cannot be eliminated but could be significantly reduced. Some of the quenching methods could be adapted to minimize residual stresses, distortion, and cracking of the material.

10.1 Interrupted Quenching Techniques

The steels are rapidly cooled from austenitizing temperature, held above M_S for a specific time, and then cooled in air. Hot oils, molten salts, and molten metals are used for this purpose.

Table 2. Thermophysical properties of various quenchants along with their wetting front velocities and average heat flux obtained while quenching with standard Inconel 600 probe

Quenchant	Thermal conductivity, W/m-k	Kinematic viscosity , mm^2/s	Solid/liquid interfacial tension, $\gamma_{lv}\cos\theta$) (mN/m	Average wetting front velocity, mm/s	Maximum average heat flux, MW/m^2	References
Water	0.594	0.975-1.52	2.52-8.45	20.94	4.81	38
5% PAG/water	0.505	1.35	8.45	33.78	5.34	
10% PAG/water	0.425	1.86	16.49	26.52	4.22	
25% PAG/water	0.302	3.70	26.71	14.18	3.71	
50% PAG/water	0.251	8.59	27.97	150	3.15	
75% PAG/water	0.234	25.82	28.72	7.305	1.703	
100% PAG	0.218	51.113	30.73	6.95	0.7191	
Brine	0.575	1.0125	3.707	44.85	5.55	64
4% PVP polymer/water	0.57	1.768	13.88	24.63	2.97	
Neem oil	0.154	100.248	37.98	8.81	1.20	65, 67
Karanja oil	0.152	62.96	36.08	6.60	1.545	
Palm oil	0.154	59	38.35	16.07	1.445	
Sunflower oil	0.151	44.34	36.86	10.68	1.63	66
Gingelly oil	0.159	60.30	37.45	15.45	1.628	
Coconut oil	0.148	42.02	35.35	18.71	1.69	
Conventional mineral oil	0.125-0.132	27.78-64.83	31.33-36.83	2.37-7.87	1.25-1.30	68
Accelerated Mineral oil	0.126-0.128	16.93-57.43	32.29-39.24	10.03-15.73	1.85-2.18	
Martempering mineral oils (hot oils)	0.135	132.13-214.542	36.28-37.86	7.01-9.67	1.63-1.82	
0.0003-0.03 wt.% MWCNT/water nanofluids	0.59-0.61	1.48-1.52	12.80-14.98	16.92-20.20	2.59-2.74	69
0.01-0.3wt.% Graphene/water nanofluids	0.53-0.61	1.50-1.55	4.61-12.96	6.47-8.54	2.44-2.61	69, 70

The isothermal cooling temperature and time depend on the type of steel and its section thickness. The objective of interrupted quenching techniques is to minimize the residual stresses due to martensitic transformation, which is the primary cause of distortion and cracking. Some of the commonly used interrupted quenching techniques are marquenching (martempering), austempering, modified marquenching, time quenching, and controlled pressure quenching (Ref 9, 94)

- Marquenching is used to achieve temperature equalization between the surface and the core of the specimen above M_S temperature to minimize the thermal gradient while proceeding through the martensite transformation stage. This will ensure that the martensite transformation will occur uniformly throughout the cross section of the specimen.
- In modified marquenching, the specimen is cooled in a quench bath maintained below the M_S temperature. It is used for the steels of low hardenability where high quench severity is required.
- In austempering, the steel is rapidly cooled from austenitizing temperature to an intermediate temperature between M_S and the nose temperature of the TTT curve. The specimen is held at that temperature for a certain time until all austenite completely transforms into bainite. Bainitic microstructure improves ductility and wear resistance. Although the hardness of bainite is lower than the martensite, the distortion produced with austempering is lower than quenching and tempering.
- Time quenching consists of rapidly cooling of the specimen in a high quench severity medium until the temperature falls below the nose of the TTT curve and then transferring to another quench medium with less quench severity where it is allowed to cool slowly in the martensite transformation range.
- Controlled pressure quenching is applied for vaporizable oil quenchants of high viscosity. The vapor film formed at the initial quenching stage is destabilized by decreasing the surface pressure of the quench medium. Thus, uniformity in cooling is improved.

10.2 Restraint Quenching Techniques

In these quenching techniques, the specimen is held in fixtures such as dies, press, and plugs. The quenchant is allowed to flow in a controlled manner. The fixtures constrain the distortion or dimensional changes. Press quenching and plug quenching are some types of restraint quenching techniques. These techniques are generally used for a specimen that undergoes high distortion in immersion quenching (Ref 9).

10.3 Intensive Quenching

Intensive quenching was developed by Kobasko in the mid-1960s. Also known as extreme quenching or shell hardening. It is based on the theory that increasing the cooling rate in the martensitic transformation range increases the tendency of

Table 3. Effect of various quenchants on the evolution of residual stress

Quenchant	Kinematic viscosity, CSt	Bath temperature, °C	Peak heat transfer coefficient, W/m^2-k	Residual stress, MPa		Remark	References	
Mineral oil (fresh)	21.4 (at 40 °C)			Hoop stress (σ_θ)	Longitudinal stress(σ_Z)		Thermal residual stress predicted at the surface of Inconel 600 Standard Probe using simulation	86
		40	3502	−146	−118			
		60	3799	−157	−128			
		80	4019	−158	−129			
		100	4026	−141	−115			
Mineral oil (oxidized)	24.03 (at 40 °C)	40	2825	−120	−96			
		60	3625	−172	−140			
		80	4013	−176	−144			
		100	4026	−162	−132			
				Φ38.1 mm × Φ50.8 mm × 10 mm 25.4 mm				
Soybean oil (SO)	31.71 (at 40 °C)	60	2471	290	125		Equivalent stress measured at the surface of AISI 4140 steel cylindrical specimens using XRD and contour drilling techniques	87, 88
Epoxidized soybean oil (ESBO)	162.77 (at 40 °C)		2314	410	250			
Fatty acid methyl esters (FAME) derived from SO	4.76 (at 40 °C)		595	210	265			
ESBO/FAME (70:30)	48.65 (at 40 °C)		635	300	115			
ESBO/FAME (62:38)	37.43 (at 40 °C)		555	90	110			
ESBO/FAME (40:60)	16.25 (at 40 °C)		517	240	160			
Houghton−Quench−G (cold quenching mineral oil)	25.25 (at 40 °C)		898	300	320			
Houghton-Quench KB (accelerated mineral oil)	13.46 (at 40 °C)		992	320	130			
				Hoop stress (σ_θ)				
Palm Oil	61(at 40 °C)	40	3921	−194			Thermal residual stress predicted at the surface of Inconel 600 Standard Probe using simulation	89
MicroTemp 157 (Slow mineral oil)	27.36 (at 40 °C)		4912	−172				
MicroTemp (153B)	40.37 (at 40 °C)		4720	−183				
				AISI 4340	AISI 1045			
Sunflower oil	31.145 (at 40 °C)	25	…	11.53	−118.34		Surface residual stress measured on the cylindrical steel samples using XRD	90
		40	…	−133.33	−310.34			
		60	…	203.92	−178.31			
		80	…	4.41	−165.91			
Soybean Oil	31.71 (at 40 °C)	25	…	−38.47	−69.99			
		40	…	−31.86	−114.46			
		60	…	−40.19	−125.62			
		80	…	−135.29	−113.84			
Mineral oil (Houghton-Quench G)	25.25 (at 40 °C)	25	…	449.76	−161.73			
		40	…	81.37	−277.49			
		60	…	236.27	−165.29			
		80	…	169.12	−111.36			
				Inner surface ($\times 10^{-3}$)		Outer surface ($\times 10^{-3}$)		
Water	0.891 (at 25 °C)	…	…	22.12		8.86	Steel tube of inner dia 2.4 mm, outer dia 5 mm and height 9 mm, equivalent residual stress predicted using simulation	91
Brine (20% w/w)	1.1120 (at 25 °C)	…	…	25		8.24		
Aqueous propylene glycol (10% w/w)	1.1952 (at 25 °C)	…	…	12.47		4.06		

quench cracking. However, there exists a critical cooling rate beyond which the cracking tendency decreases. In this method, the surface of the heated specimen is cooled uniformly with a very high cooling rate. As a result, the austenite at the surface transforms instantaneously into martensite, creating a hardened shell. A very high compressive residual stress at the surface layer is created during the transformation from austenite to martensite. The hardened shell formed at the surface resists the stresses due to thermal shrinkage and phase transformation at the core, thereby minimizing distortion (Ref 96). For intensive quenching, the Grossmann quench severity number should be greater than 6 (Ref 97) and the HTC in the range of 20,000-50,000 W/m^2K (Ref 98).

The intensive quenching (IQ) is categorized into IQ-1, IQ-2, and IQ-3 based on the mode of heat transfer at the metal/quenchant interface. IQ-1 consists of both film and nucleate boiling. The cooling in IQ-2 is through nucleate boiling and convective cooling, and IQ-3 consists of only convective cooling heat transfer. IQ-1 is a two-step process in which the component is initially cooled slowly from austenitic temperature to M_S by quenching in oil or polymer solution. The component is then transferred to an intensive quenching chamber where intense cooling is performed by directing a stream of water or water jets onto the specimen surface. The intense cooling in the M_S–M_f region yields a hardened outer shell with high compressive stresses at the surface with the tough and ductile core. IQ-2 is a three-step process where the component is rapidly cooled from austenitic temperature until 50% martensite transformation occurs at the surface. The cooling is interrupted by taking the component out and cooling it in air.

At this stage, the hardened outer shell undergoes self-tempering by the heat released from the core. Finally, the component is returned back in quench tank for convective cooling. For avoiding film boiling at the initial cooling stage, the water is mixed with salt in low concentration. However, the requirement for IQ-2 is that the boiling temperature of the quenchant should be more or less equal to the temperature corresponding to 50% martensite transformation of the steel. IQ-3 overcomes the demerits of IQ-1 and IQ-2, being a single stage quenching process. Convective cooling is performed by providing a uniform and intense water flow/water jet to cool the surface. High compressive stress at the surface could be achieved with an optimum depth of the hardened shell. IQ-1 applies to high and medium alloyed steel parts whereas IQ-2 and IQ-3 can be applied to low alloyed steel (Ref 99).

Intensive quenching has a number of advantages such as minimizing distortion and cracking, improvement in mechanical properties of steel due to the high surface compressive residual stresses, the possibility of case hardening low alloyed steels and thereby eliminating the process of carburizing and quenching, and finally minimizing the use of hazardous quench oils. However, intensive quenching has few limitations. The component's part geometry and section thickness play a major role in the heat transfer and hardening effect. It is extremely difficult to direct the water jet or stream of water to flow uniformly over an intricately shaped component. For components with section thickness less than 6mm, it is difficult to create a hardened outer shell with soft core. Batch quenching cannot be performed in an intensive quenching process (Ref 99-101). Case studies on the application of intensive quenching on plane carbon, alloyed steels, and industrial components such as coil springs, forklift forks, and bearing cages are provided in the literature (Ref 102-104). It is observed that the intensively quenched component showed minimum distortion, superior mechanical properties, improvement in fatigue life, and corrosion resistance.

10.3.1 Use of Water-Salt and Water-Polymer Quenchants with Intense Cooling Effects. Kobasko et al. (Ref 105-109) investigated the use of forced convection utilizing shock boiling phenomena to avoid the vapor blanket stage during quenching. Water-salt electrolyte and water-inverse soluble polymer quench medium having optimum polymer concentration as low as 1% were used. The authors suggested that while quenching in an electrolyte, the specimen should be negatively charged, creating a charged layer over the surface. The free-electron exerts an electrical force that pulls the liquid layer toward the surface. Hence a periodic film and shock boiling exist that results in intensive cooling. The 1% polymer/water quenchant created a thin insulating polymer layer over the specimen surface just enough to avoid the film boiling stage. The breakage of the polymer film was uniform and intensive to create shock boiling phenomena. The quenchants were used with a hydrodynamic emitter that created a resonance effect to break the vapor film during quenching. The combination of optimal concentration of salt/polymer with water and the resonance effect resulted in an intensive cooling where the initial film boiling stage was completely absent. The heat transfer occurred only through nucleate boiling and convective cooling stages. As a result of the absence of vapor film, the heat transfer was accelerated, and the uniformity of heat transfer was improved. The accelerated heat transfer led to forming a hardened outer case with high compressive residual stresses and super strengthening of the quenched sample. The authors further suggested that using this mechanism, optimal hardenability steel could be case hardened to a level equivalent to the carburization process, and the depth of case hardening could be controlled. Thus, the expense of addition of alloying elements and the carburization process could be minimized in addition to distortion.

10.4 Use of Ionic Liquids as Quench Media

Beck et al. (Ref 110-112) introduced ionic liquids or molten salts with melting temperatures less than 100 °C as quenchants for quenching steels and aluminum alloys. The ionic liquids used were 1-ethyl-3-methylimidazolium ethyl sulfate and 1-ethyl-3-methylimidazolium bis (trifluoromethyl sulfonyl) imide. The results indicated that quenching in ionic liquid showed very little or no film boiling stage and the uniformity of heat transfer was higher than water. The cooling rates of the ionic liquids were increased by adding volatile liquids like water and ethanol up to a concentration of 10% w/w. Moreover, ionic liquids showed higher thermal stability. The volatile decomposition in ionic liquids, even after repeated use, was only 1%. Furthermore, the distortion of an aluminum specimen of complex geometry while quenching in ionic liquids was studied. It was observed that quenching in ionic liquid showed a low specimen distortion compared to water and mineral oil.

Table 4. Percentage distortion attained with various quenchants using Navy C-ring test

Quenchant	Steel grade	% Distortion	References
Water	65Mn steel	3.606	92
10% PAG polymer/water		1.202	
20% PAG polymer/water		0.817	
Oil		0.795	
Soybean Oil (SO)	AISI 4140	3.75	87
Epoxidized Soybean oil (ESBO)		3.5	
Fatty Acid Methyl Esters (FAME) derived from SO		4.5	
ESBO/FAME (70:30)		2.7	
ESBO/FAME (62:38)		3.25	
ESBO/FAME (40:60)		4.6	
Houghton-Quench-G (cold quenching mineral oil)		4.0	
Houghton-Quench KB (accelerated mineral oil)		2.2	

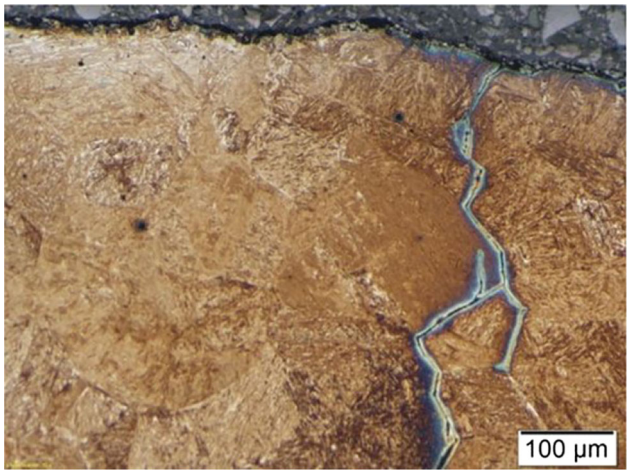

Fig. 20. Intergranular crack propagation in the grain boundaries due to sulfide inclusion in a quenched and tempered high carbon tool steel. Reprinted from *Engineering Failure Analysis,* Vol 92, S. Šolić, B. Podgornik, V. Leskovšek, The Occurrence of Quenching Cracks in High-Carbon Tool Steel Depending on the Austenitizing Temperature, Pages 140-148, Copyright 2018, with permission from Elsevier [93]

Fig. 21. Quench crack observed in AISI 52100 steel while quenching in distilled water and carbonated water. Reprinted by permission from Springer Nature Customer Service Centre GmbH: Springer Nature, *Transactions of the Indian Institute of Metals,* Comparison of Cooling Behaviour of Carbon Steels in Polymer, Oil and Carbonated Quench Media, N.G. Mathews, K.M.P. Rao, U.V. Nayak, K.N. Prabhu, Copyright 2019 [95]

11. Conclusions

Quench hardening heat treatment involves simultaneous occurrence of physical events such as heat transfer from the heated metal to the quench medium, phase transformation, and the evolution of stresses and strain in the material. The interfacial heat transfer from the metal surface to the quench medium controls the last two physical events. The metal/quenchant interfacial heat transfer occurs through three stages: film boiling, nucleate boiling, and convective cooling. The delayed transition from the film to the nucleate stage and the rewetting phenomenon decide the nonuniformity in heat transfer. The nonuniform heat transfer creates a thermal gradient across the specimen, leading to a differential thermal expansion and variation in the volume fraction of martensite, resulting in thermal and transformation residual stresses. The nonuniformity in heat transfer depends on the geometry of the specimen and the rewetting kinematics exhibited by the quench medium being used. Understanding the rewetting kinematics of the quench medium and quantifying the nonuniformity of heat transfer is essential for the proper selection of quenchants for hardening steel components with specific geometry and hardenability. Modeling quench hardening involves simultaneous analysis of heat transfer, mechanical and metallurgical models. The heat transfer provides the temperature distribution inside the specimen, while the metallurgical and mechanical models predict the microstructural evolution and stress–strain distribution respectively. Successful simulation of residual stress and distortion during quenching requires accurate modeling of metal/quenchant interfacial heat transfer and a reliable database on the temperature dependent thermophysical properties of the material and the quench medium.

The following is the outcome of the present review of the literature.

1. During quenching, residual thermal and transformation stresses fluctuate at the surface and the core from tensile to compressive and vice versa. The final residual stress distribution depends on whether the start of martensitic transformation occurs before/after or at the same time as the inversion of residual thermal stress. Based on the initiation time of martensitic transformation, the residual stress distribution in steels are classified into thermal, transitional, and transformation types. The stress distribution is significantly influenced by the section thickness of the component and the type of quenchant.

2. The current research work involving the simulation of quenching mostly uses a constant value of heat transfer coefficient (HTC) to model the temperature distribution. Using spatiotemporal heat transfer coefficient to model the temperature field incorporating the effect of rewetting kinetics and kinematics would improve the accuracy of residual stress distribution.
3. Estimation of the spatiotemporal HTC/ heat flux could be done for various steel/quenchant combinations using the IHCP method. The method estimates the interfacial heat flux by using the measured cooling curves within the specimen. CFD analysis along with empirical boiling heat transfer correlations could be integrated to the quenching simulation for the estimation of HTC. However, for this purpose, the thermophysical properties of the quench media have to be known.
4. A uniformity parameter must be defined for a quenchant indicating the uniformity of heat transfer. A database on the quenchant's uniformity, severity and HTC would benefit heat-treaters in selecting a quench medium to minimize residual stress and distortion. An artificial neural network (ANN) model would be of great utility in predicting the type of quench medium required for quenching a particular steel grade.
5. The rewetting or the wetting front velocity significantly affects the magnitude and uniformity of metal/quenchant interfacial heat flux. The increase in wetting front velocity increased the magnitude of heat flux. Very high and low wetting front velocity caused significant spatial nonuniformity of heat flux.
6. The wetting front velocity is an inherent property of the quenchant and varies significantly with the kinematic viscosity and the solid/liquid interfacial tension. The wetting front velocity showed an exponential decrease with increase in viscosity and a linear decrease with increase in interfacial tension.
7. The effect of thermophysical properties of quenchants on the magnitude of heat flux indicated that the heat flux increased with increase in thermal conductivity and decreased with increase in kinematic viscosity and solid/liquid interfacial tension.
8. Distortion during quenching could be significantly minimized using alternative quenching methods such as intensive quenching. The HTCs estimated in this method are of the order 20,000-50,000 W/m^{2}K. The technique minimizes distortion and improves the mechanical properties of the steel component.
9. Quenching in liquids that show minimum or no film boiling stage improved heat transfer uniformity. The presence of high molecular weight triglyceride molecules in vegetable oils increased the boiling temperature, indicating a minimum or no film boiling stage. Heat transfer in ionic liquids or molten salts occurs in two stages only, and the film boiling stage is absent.

References

1. H.M. Tensi, A. Stich and G.E. Totten, Quenching and Quenching Technology, *Steel Heat Treatment Handbook*, 2nd ed., G.E. Totten Ed., CRC Press, Boca Raton, 2006, p 551
2. C. Simsir and C.H. Gur, Simulation of Quenching, *Handbook of Thermal Process Modeling Steels*. C.H. Gur, J. Pan Ed., CRC Press, Boca Raton, 2008, p 341. https://doi.org/10.1201/9781420003581
3. S. Kamamoto, T. Nishimori and S. Kinoshita, Analysis of Residual Stress and Distortion Resulting from Quenching in Large Low-Alloy Steel Shafts, *Mater. Sci. Technol. (United Kingdom)*, 1985, **1**(10), p 798–804. https://doi.org/10.1179/mst.1985.1.10.798
4. D.E. Lozano, G.E. Totten, Y. Bedolla-Gil, M. Guerrero-Mata, M. Carpio and G.M. Martinez-Cazares, X-ray Determination of Compressive Residual Stresses in Spring Steel Generated by High-Speed Water Quenching, *Materials*, 2019 https://doi.org/10.3390/ma12071154
5. N.A. Noda, K. Hu, Y. Sano, K. Ono and Y. Hosokawa, Usefulness of Non-Uniform Heating and Quenching Method for Residual Stress of Bimetallic Roll: FEM Simulation Considering Creep Behavior, *Steel Res. Int.*, 2017, **88**(3), p 1–11. https://doi.org/10.1002/srin.201600165
6. X. Zhao, P. Munroe, D. Habibi and Z. Xie, Roles of Compressive Residual Stress in Enhancing the Corrosion Resistance of Nano Nitride Composite Coatings on Steel, *J. Asian Ceram. Soc.*, 2013, **1**(1), p 86–94. https://doi.org/10.1016/j.jascer.2013.03.002
7. W. Wang, H. Liu, C. Zhu, P. Bocher, H. Liu and Z. Sun, Evaluation of Rolling Contact Fatigue of a Carburized Wind Turbine Gear Considering The Residual Stress and Hardness Gradient, *J. Tribol.*, 2018, **140**(6), p 1–10. https://doi.org/10.1115/1.4040052
8. T. Croucher, Using Polyalkylene Glycol Quenchants to Effectively Control Distortion and Residual Stresses in Heat Treated Aluminum Alloys, *ASTM Spec. Tech. Publ.*, 2010, **1523**(10), p 309–331. https://doi.org/10.1520/stp49157s
9. L.C.F. De Canale and G.E. Totten, Overview of Distortion and Residual Stress Due to Quench Processing Part I: Factors Affecting Quench Distortion, *Int. J. Mater. Prod. Technol.*, 2005, **24**(1–4), p 4–52. https://doi.org/10.1504/ijmpt.2005.007941
10. C. Márquez, E. Martínez, J. Cárdenas, O. Saldívar, J. Rodríguez, F. Fernández and A. Pérez, Study of the Impact of Quenching Process Parameters in High Dimension Rings of Steel AISI 4140, *Mater. Res. Soc. Symp. Proc.*, 2012, **1372**, p 151–156. https://doi.org/10.1557/opl.2012.121
11. X. Luo and G.E. Totten, Evolution From Cooling Modeling to Cooling Engineering of the Steel Quenching Process: a Technology Overview, *Mater. Perform. Charact.*, 2018, **8**(2), p 213–240. https://doi.org/10.1520/MPC20180028
12. G.E. Totten and L.L.M. Albano, IFHTSE Global 21: Heat Treatment and Surface Engineering in the Twenty-First Century, *Int. Heat Treat. Surf. Eng.*, 2012, **6**(1), p 4–14. https://doi.org/10.1179/1749514811Z.0000000001
13. ASM Heat Treating Society, ASM Heat Treating Society's 1999 Research and Development Plan (ASM International, Materials Park, 1997)
14. HTS Heat Treating Society, ASM International. https://www.asminternational.org/web/hts/about/future. Accessed 22 Sep 2021
15. H. Krause and H.H. Jühe, Internal Stresses During Rolling Friction and Their Evaluation, *Wear*, 1977, **41**(1), p 15–23. https://doi.org/10.1016/0043-1648(77)90188-0
16. V. Schulze, O. Vohringer and E. Macherauch, Residual Stresses After Quenching, *Quenching Theory and Technology*, 2nd ed., B. Liscic, H.M. Tensi, L.C.F. Canale, G.E. Totten Ed., CRC Press, Boca Raton, 2010, p 229. https://doi.org/10.1201/9781420009163
17. C. Simsir and C.H. Gur, A Review on Modeling and Simulation of Quenching, *J. ASTM Int.*, 2009, **6**(2), p 1–29. https://doi.org/10.1520/JAI101766
18. F.D. Fischer, Q.-P. Sun and K. Tanaka, Transformation-Induced Plasticity (TRIP), *Appl. Mech. Rev.*, 1996, **49**(6), p 317–364. https://doi.org/10.1115/1.3101930
19. C. Simsir and C.H. Gur, Simulation of Quenching, *Quenching Theory and Technology*, 2nd ed., B. Liscic, H.M. Tensi, L.C.F. Canale, G.E. Totten Ed., CRC Press, Boca Raton, 2010, p 605
20. M. Avrami, Kinetics of Phase Change. I: General Theory, *J. Chem. Phys.*, 1939, **7**(12), p 1103–1112. https://doi.org/10.1063/1.1750380
21. J.W. Cahn, Transformation Kinetics During Continuous Cooling, *Acta Metall.*, 1956, **4**(6), p 572–575. https://doi.org/10.1016/0001-6160(56)90158-4
22. J.W. Christian, *The Theory of Transformations in Metals and Alloys Part 1*, 3rd ed. Pergamon Press, London, 2002

23. M.C. Weinberg, D.P. Birnie and V.A. Shneidman, Crystallization Kinetics and the JMAK Equation, *J. Non. Cryst. Solids.*, 1997, **219**, p 89–99. https://doi.org/10.1016/S0022-3093(97)00261-5
24. D.P. Koistinen and R.E. Marburger, A General Equation Prescribing the Extent of the Austenite-Martensite Transformation in Pure Iron-Carbon Alloys and Plain Carbon Steels, *Acta Metall.*, 1959, **7**(1), p 59–60. https://doi.org/10.1016/0001-6160(59)90170-1
25. G.E. Dieter, *Mechanical Metallurgy*, McGraw-Hill Book Co., Ltd., London, 1988
26. Z. Li, B.L. Ferguson, V. Nemkov, R. Goldstein, J. Jackowski and G. Fett, Effect of Quenching Rate on Distortion and Residual Stresses During Induction Hardening of a Full-Float Truck Axle Shaft, *J. Mater. Eng. Perform.*, 2014, **23**(12), p 4170–4180. https://doi.org/10.1007/s11665-014-1196-0
27. S. Hossain, C.E. Truman, D.J. Smith and M.R. Daymond, Application of Quenching to Create Highly Triaxial Residual Stresses in Type 316H Stainless Steels, *Int. J. Mech. Sci.*, 2006, **48**(3), p 235–243. https://doi.org/10.1016/j.ijmecsci.2005.11.002
28. S.N. Lingamanaik and B.K. Chen, Thermo-Mechanical Modelling of Residual Stresses Induced by Martensitic Phase Transformation and Cooling During Quenching of Railway Wheels, *J. Mater. Process. Technol.*, 2011, **211**(9), p 1547–1552. https://doi.org/10.1016/j.jmatprotec.2011.04.007
29. S.N. Lingamanaik and B.K. Chen, The Effects of Carburising and Quenching Process on the Formation of Residual Stresses in Automotive Gears, *Comput. Mater. Sci.*, 2012, **62**, p 99–104. https://doi.org/10.1016/j.commatsci.2012.05.033
30. R. Masoudi Nejad, Using Three-Dimensional Finite Element Analysis for Simulation of Residual Stresses in Railway Wheels, *Eng. Fail. Anal.*, 2014, **45**, p 449–455. https://doi.org/10.1016/j.engfailanal.2014.07.018
31. A.J. Fletcher and A.B. Soomro, The Generation of Thermal Stress and Strain During the Quenching of Steel Plates in Polyalkylene Glycol, *Mater. Sci. Eng.*, 1987, **91**, p 153–160. https://doi.org/10.1016/0025-5416(87)90293-X
32. K.F. Wang and H.T.Y. Yang, Experimental and Computational Study of the Quenching of Carbon Steel, *J. Manuf. Sci. Eng. Trans. ASME*, 1997, **119**(3), p 257–265. https://doi.org/10.1115/1.2831102
33. W. Zhang, Z. De Qu, X.H. Deng and X.W. Duan, Numerical Simulation of Cr12MoV Steel During Quenching Process, *Adv. Mater. Res.*, 2014, **989–994**, p 751–754. https://doi.org/10.4028/www.scientific.net/AMR.989-994.751
34. A.K. Esfahani, M. Babaei and S.S. Foroushani, A Numerical Model Coupling Phase Transformation to Predict Microstructure Evolution and Residual Stress During Quenching of 1045 Steel, *Math. Comput. Simul.*, 2021, **179**, p 1–22. https://doi.org/10.1016/j.matcom.2020.07.016
35. S. Brunbauer, G. Winter, T. Antretter, P. Staron and W. Ecker, Residual Stress and Microstructure Evolution in Steel Tubes for Different Cooling Conditions-Simulation and Verification, *J. Mater. Sci. Eng. A*, 2019, **747**, p 73–79. https://doi.org/10.1016/j.msea.2019.01.037
36. Y. Liu, S. Qin, J. Zhang, Y. Wang, Y. Rong, X. Zuo and N. Chen, Influence of Transformation Plasticity on the Distribution of Internal Stress in Three Water-Quenched Cylinders, *Metall. Mater. Trans. A Phys. Metall. Mater. Sci.*, 2017, **48**(10), p 4943–4956. https://doi.org/10.1007/s11661-017-4230-7
37. B.H. Morales, H.J.V. Hernandez, G.S. Diaz and G.E. Totten, Experimental and Computational Study of Heat Transfer During Quenching of Metallic Probes, *Evaporation, Condensation and Heat Transfer*. A. Ahsan Ed., IntechOpen, London, 2011, p 49–72. https://doi.org/10.5772/24469
38. G. Ramesh and K.N. Prabhu, Effect of Polymer Concentration on Wetting and Cooling Performance During Immersion Quenching, *Metall. Mater. Trans. B*, 2016, **47B**, p 859–881. https://doi.org/10.1007/s11663-015-0541-5
39. K.N. Prabhu and A.A. Ashish, Inverse Modeling of Heat Transfer with Application to Solidification and Quenching, *Mater. Manuf. Processes*, 2002, **17**(4), p 469–481. https://doi.org/10.1081/AMP-120014230
40. M.N. Ozisik and H.R.B. Orlande, *Inverse Heat Transfer Fundamentals and Applications*, CRC Press, Boca Raton, 2000, p 35–111
41. T.S.P. Kumar, A Serial Solution for the 2-D Inverse Heat Conduction Problem for Estimating Multiple Heat Flux Components, *Numer. Heat Transf. Part B*, 2004, **45**, p 541–563. https://doi.org/10.1080/10407790490277940
42. K.M.P. Rao and K.N. Prabhu, Effect of Bath Temperature on Cooling Performance of Molten Eutectic $NaNO_3$-KNO_3 Quench Medium for Martempering of Steels, *Metall. Mater. Trans. A*, 2017, **48A**, p 4895–4904. https://doi.org/10.1007/s11661-017-4267-7
43. J. Jan and D.S. MacKenzie, On the Development of Parametrical Water Quenching Heat Transfer Model Using Cooling Curves by ASTM D6200 Quenchometer, *J. Mater. Eng. Perform.*, 2020, **29**(6), p 3612–3625. https://doi.org/10.1007/s11665-020-04803-z
44. L.A. Bromley, *Heat Transfer in Stable Film Boiling*, Dissertation, (University of California, Los Angeles, 1948)
45. N. Zuber, *Hydrodynamic Aspects of Boiling Heat*, Dissertation (University of California, Los Angeles, 1959)
46. P.J. Berenson, Film-Boiling Heat Transfer from a Horizontal Surface, *J. Heat Transf.*, 1961, **83**(3), p 351–356. https://doi.org/10.1115/1.3682280
47. T.C. Hua and J.J. Xu, Quenching Boiling in Subcooled Liquid Nitrogen for Solidification of Aqueous Materials, *Mater. Sci. Eng. A*, 2000, **292**(2), p 169–172. https://doi.org/10.1016/S0921-5093(00)01004-2
48. W.J.J. Vorster, M.W. Van Der Watt, A.M. Venter, E.C. Oliver, D.G.L. Prakash and A.M. Korsunsky, Influence of Quenchant Hydrodynamics and Boiling Phase Incipient Temperature Shifts on Residual Stress Formation, *Heat Transf. Eng.*, 2009, **30**(7), p 564–573. https://doi.org/10.1080/01457630802594937
49. I. Medina-Juárez, J. Araujo De Oliveira, R.J. Moat and F.A. García-Pastor, On the Accuracy of Finite Element Models Predicting Residual Stresses in Quenched Stainless Steel, *Metals*, 2019, **9**(12), p 1–16. https://doi.org/10.3390/met9121308
50. B. Yegnanarayana, *Artificial Neural Networks*, New Delhi, PHI Learning Private Limited, 2019, p 15–75
51. Y. Bouissa, D. Shahriari and H. Champliaud, Jahazi M (2019) Prediction of Heat Transfer Coefficient during Quenching of Large Size Forged Blocks Using Modeling and Experimental Validation, *Case Stud Therm Eng*, 2018, **13**, p 100379. https://doi.org/10.1016/j.csite.2018.100379
52. M. Toparli, S. Sahin, E. Ozkaya and S. Sasaki, Residual Thermal Stress Analysis in Cylindrical Steel Bars Using Finite Element Method and Artificial Neural Networks, *Comput. Struct.*, 2002, **80**(23), p 1763–1770. https://doi.org/10.1016/S0045-7949(02)00215-8
53. S.S. Hanza, T. Marohnić, D. Iljkić and R. Basan, Artificial Neural Networks-Based Prediction of Hardness of Low-Alloy Steels Using Specific Jominy Distance, *Metals (Basel)*, 2021 https://doi.org/10.3390/met11050714
54. K.M.P. Rao and K.N. Prabhu, Numerical Simulation to Predict the Effect of Process Parameters on Hardness during Martempering of AISI4140 Steel, *J. Mater. Eng. Perform.*, 2021, **30**(5), p 3416–3435. https://doi.org/10.1007/s11665-021-05630-6
55. L.C.F. Canale and M. Narazaki, Quenching and Cooling, Residual Stress and Distortion Control, *J. ASTM Int. STP*, 2010 https://doi.org/10.1520/STP1523-EB
56. G. Ramesh and K.N. Prabhu, Assessment of the Effect of the Quench Probe Parameters on Cooling Behavior by Numerical Simulation, *Procedia Mater. Sci.*, 2014, **5**, p 1314–1321. https://doi.org/10.1016/j.mspro.2014.07.448
57. U.V. Nayak and K.N. Prabhu, Effect of Section Thickness on Heat Transfer During Quenching in Vegetable Oils, *Mater. Perform. Charact.*, 2018, **7**(1), p 384–396. https://doi.org/10.1520/MPC20180084
58. U.V. Nayak and K.N. Prabhu, Quenching Cooling Performance-Hardness Correlation for AISI 1045 and 1090 steels, *Mater. Perform. Charact.*, 2019, **8**(1), p 135–150. https://doi.org/10.1520/MPC20180138
59. K. Babu, Effect of Part Size on Surface Heat Flux during Immersion Quenching, *Adv. Mater. Res.*, 2012, **488–489**, p 353–357. https://doi.org/10.4028/www.scientific.net/AMR.488-489.353
60. G. Ramesh and K.N. Prabhu, Effect of Boundary Heat Transfer Coefficient and Probe section Size on Cooling curves during Quenching, *Mater. Perform. Charact.*, 2012, **1**(1), p 1–8. https://doi.org/10.1520/MPC104365
61. C.H. Gür, Investigation of the Influence of Specimen Geometry on Quench Behaviour of Steels by X-ray Determination of Surface

Residual Stresses, *Int. J. Mech. Sci.*, 2002, **44**(7), p 1335–1347. https://doi.org/10.1016/S0020-7403(02)00051-6
62. C. Şimşir and C.H. Gür, 3D FEM Simulation of Steel Quenching and Investigation of the Effect of Asymmetric Geometry on Residual Stress Distribution, *J. Mater. Process. Technol.*, 2008, **207**(1–3), p 211–221. https://doi.org/10.1016/j.jmatprotec.2007.12.074
63. G. Ramesh and K.N. Prabhu, Assessment of Axial and Radial Heat Transfer During Immersion Quenching of Inconel Probe, *Exp. Therm. Fluid Sci.*, 2014, **54**, p 158–170. https://doi.org/10.1016/j.expthermflusci.2014.01.016
64. G. Ramesh and K.N. Prabhu, Spatial Dependence of Heat Flux Transients and Wetting Behavior During Immersion Quenching of Inconel 600 Probe in Brine and Polymer Media, *Metall. Mater. Trans. B*, 2014, **45B**, p 1355–1369. https://doi.org/10.1007/s11663-014-0038-7
65. U.V. Nayak and K.N. Prabhu, Heat Transfer During Quenching of Inconel Probe in Non-edible Vegetable Oils, *HTM J. Heat Treatm. Mat.*, 2018, **73**(5), p 283–291. https://doi.org/10.3139/105.110365
66. G. Ramesh and K.N. Prabhu, Wetting and Cooling Performance of Vegetable Oils During Quench Hardening, *Heat Transf. Asian Res.*, 2014, **45**(4), p 342–357. https://doi.org/10.1002/htj.21165
67. G. Ramesh and K.N. Prabhu, Wetting Kinetics, Kinematics and Heat Transfer Characteristics of Pongamia Pinnata Vegetable Oil for Industrial Heat Treatment, *Appl. Therm. Eng.*, 2014, **65**(1–2), p 433–446. https://doi.org/10.1016/j.applthermaleng.2014.01.011
68. G. Ramesh and K.N. Prabhu, Wetting and Cooling Performance of Mineral Oils for Quench Heat Treatment of Steels, *ISIJ Int.*, 2014, **54**(6), p 1426–1435. https://doi.org/10.2355/isijinternational.54.1426
69. U.V. Nayak and K.N. Prabhu, Wetting Behavior and Heat Transfer of Aqueous Graphene Nanofluids, *J. Mater. Eng. Perform.*, 2016, **25**, p 1474–1480. https://doi.org/10.1007/s11665-016-1962-2
70. U.V. Nayak and K.N. Prabhu, Heat Transfer During Quenching in Graphene and Multiwall Carbon Nanotube Nanofluids Under Agitated Quench Conditions, *J. Nanofluids*, 2019, **8**(6), p 1222–1239. https://doi.org/10.1166/jon.2019.1680
71. U.V. Nayak and K.N. Prabhu, Heat Transfer and Quench Performance of Aqueous CuO Nanofluids During Immersion Quenching, *Int. J. Microstruct. Mater. Prop.*, 2016, **11**(3/4), p 186–202. https://doi.org/10.1504/IJMMP.2016.079139
72. G. Ramesh and K.N. Prabhu, The Effect of Addition of Copper Nanoparticles on Wetting Behavior of Water During Immersion Quenching, *Trans. Indian Inst. Met.*, 2013, **66**, p p375-379. https://doi.org/10.1007/s12666-013-0278-2
73. P. Keblinski, S.R. Phillpot, S.U.S. Choi and J.A. Eastman, Mechanism of Heat Flow in Suspensions of Nano-Sized Particles (Nanofluids), *Int. J. Heat Mass Transf.*, 2002, **45**, p 855–863. https://doi.org/10.1016/S0017-9310(01)00175-2
74. H. Kim, J. Buongiorno, L.W. Hu, and T. McKrell, *Effect of Nanoparticle Deposition on Rewetting Temperature and Quench Velocity in Experiments with Stainless Steel Rodlets and Nanofluids*, in *Proceedings of the 7th International Conference on Nanochannels, Microchannels, Minichannels 2009, ICNMM2009, 2009, (PART A)*, p 25–30. https://doi.org/10.1115/ICNMM2009-82082
75. K.M.P. Rao and K.N. Prabhu, Assessment of Cooling Performance of Neem Oil for Distortion Control in Heat Treatment of Steel, *J. Mater. Eng. Perform.*, 2020, **29**, p 6033–6043. https://doi.org/10.1007/s11665-020-05082-4
76. K.M.P. Rao and K.N. Prabhu, A Comparitive Study on Cooling Performance of Hot Oil and Molten Salt Quench Media for Industrial Heat Treatment, *J. Mater. Eng. Perform.*, 2020, **29**, p 3494–3501. https://doi.org/10.1007/s11665-020-04635-x
77. K.M.P. Rao and K.N. Prabhu, Compositional and Bath Temperature Effects on Heat Transfer During Quenching in Molten $NaNO_3$-KNO_3 Salt Mixtures, *J. Mater. Eng. Perform.*, 2020, **29**, p 1860–1868. https://doi.org/10.1007/s11665-020-04692-2
78. R.D. López-García, F.A. García-Pastor, A. Maldonado-Reyes, M.A. Jiménez-Gómez and J.A. Rodríguez-García, Analysis of the Effect of Immersion Rate on the Distortion and Residual Stresses in Quenched SAE 5160 Steel using FEM, *J. Mater. Res. Technol.*, 2019, **8**(6), p 5557–5571. https://doi.org/10.1016/j.jmrt.2019.09.024
79. M. Sedighi and C.A. McMahon, The Influence of Quenchant Agitation on the Heat Transfer Coefficient and Residual Stress Development in the Quenching of Steels, *Proc. Inst. Mech. Eng. Part B*, 2000, **214**(7), p 555–567. https://doi.org/10.1243/0954405001518251
80. M.M. Nunes, E.M. Da Silva, R.A. Renzetti and T.G. Brito, Analysis of Quenching Parameters in AISI 4340 Steel by using Design of Experiments, *Mater. Res.*, 2018, **22**(1), p 1–7. https://doi.org/10.1590/1980-5373-MR-2018-0315
81. R. Jeschar, E. Specht and C. Köhler, Heat Transfer During Cooling of Heated Metals with Vaporizable Liquids, *Quenching Theory and Technology*, 2nd ed., B. Liscic, H.M. Tensi, L.C.F. Canale, G.E. Totten Ed., CRC Press, Boca Raton, 2010, p 159. https://doi.org/10.1201/9781420009163
82. "Standard Test Method for Determination of Cooling Characteristics of Quench Oils by Cooling Curve Analysis", ASTM D6200-01, ASTM International (West Conshocken, USA, 2012)
83. K.N. Prabhu and G. Ramesh, A Dimensional Parameter for Prediction of Cooling Performance of Quenchants, *Mater. Perform. Charact.*, 2014, **3**(4), p 242–255. https://doi.org/10.1520/MPC20140002
84. K.N. Prabhu and P. Fernandes, Effect of Surface Roughness on Metal/Quenchant Interfacial Heat Transfer and Evolution of Microstructure, *Mater. Des.*, 2007, **28**, p 544–550. https://doi.org/10.1016/j.matdes.2005.08.005
85. R.L. Simencio Otero, L.C.F. Canale, G.E. Totten and L. Meekisho, Vegetable Oils as Metal Quenchants: A Comprehensive Review, *Mater. Perform. Charact.*, 2017, **6**(1), p 174–250. https://doi.org/10.1520/mpc20160112
86. R. N. Penha, L. C. F. Canale, U. D. S. Paulo, S. Carlos, G. E. Totten, *Simulation of Heat Transfer Properties and Residual Stress Analyses of Cooling Curves Obtained from Quenching Studies*, SAE Tech. Pap. Ser. E., (2005). https://doi.org/10.4271/2005-01-4178
87. C. Civera, B. Rivolta, R.L. Simencio-Otero, J.G. Lúcio, G.E. Totten and L.C.F. Canale, Vegetable Oils as Quenchants for Steels: Residual Stresses and Dimensional Changes, *Mater. Perform. Charact.*, 2014, **3**(4), p 306–325. https://doi.org/10.1520/MPC20140039
88. C. Civera, B. Rivolta, R. L. S. Otero, J. G. Lucio, L. C. F. Canale, G. E. Totten, *Study of Residual Stresses after Quenching with Vegetable Oils*, in Proceedings of the 23rd IFHTSE Congr., April 18–21 (Savannah, 2016), p 361–367
89. D.S. Schicchi, G. Belinato, G.S. Sarmiento, A. Gastón, G.E. Totten, and L.C.F. Canale, *Effect of Soybean Oil and Palm Oil Oxidation Stability on the Variation of Heat Transfer Coefficients and Residual Stress*, in *Quenching Control Distortion—Proceedings of the 6th International Quenching Control Distortion Conference Incl. 4th International Distortion Engineering Conference, 2012* (2016) p 621–633
90. P. Brito, P.A. Ramos, L.P. Resende, D.A. de Faria and O.K. Ribas, Experimental Investigation of Cooling Behavior and Residual Stresses for Quenching with Vegetable Oils at Different Bath Temperatures, *J. Clean. Prod.*, 2019, **216**, p 230–238. https://doi.org/10.1016/j.jclepro.2019.01.194
91. P. Sarker, U. K. Chakravarty, *Analysis of the Residual Stress and Deformation in a Steel Tube due to Quenching Process using Different Media*, in *Proceedings of the ASME International Mechanical Engineering Congress Exposition* (Montreal, 2014)
92. T.X. Tran, X.P. Nguyen, D.N. Nguyen, D.T. Vu, M.Q. Chau, O.I. Khalaf and A.T. Hoang, Effect of Poly-Alkylene-Glycol Quenchant on the Distortion, Hardness, and Microstructure of 65Mn Steel, *Comput. Mater. Contin.*, 2021, **67**(3), p 3249–3264. https://doi.org/10.32604/cmc.2021.015411
93. S. Šolić, B. Podgornik and V. Leskovšek, The Occurrence of Quenching Cracks in High-Carbon Tool Steel Depending on the Austenitizing Temperature, *Eng. Fail. Anal.*, 2018, **92**, p 140–148. https://doi.org/10.1016/j.engfailanal.2018.05.008
94. G. E. Totten, G. E. Totten and Associates LLC, M. Narazaki(Utsunomiya University, Japan), R. R. Blackwood, L. M. Jarvis(Tenaxol Inc.), Failure Related To Heat Treatment Operations, Failure Analysis and Prevention Volume 11 (ASM International, 2002), p 399–482
95. N.G. Mathews, K.M.P. Rao, U.V. Nayak and K.N. Prabhu, Comparison of Cooling Behaviour of Carbon Steels in Polymer, Oil and Carbonated Quench Media, *Trans. Indian Inst. Met.*, 2019, **72**(6), p 1405–1408. https://doi.org/10.1007/s12666-018-1542-2
96. M. Aronov, N. Kobasko, J. Powell, B. Andreski, B. O'Rourke, *Intensive Quenching Processes: Basic Principles, Applications and Commercialization*, in *Proceedings of the European Conference on Heat Treatment 21st IFHTSE Congress, 2014* (Munich, Germany), p 267–274

97. Industrial Heating, Overview of Intensive Quenching Process, 2002, https://www.industrialheating.com/articles/83971-overview-of-intensive-quenching-processes. Accessed 09 Dec 2021
98. F. Frerichs, T. Lubben, F. Hoffmann and H.W. Zoch, Shell Hardening of Unalloyed Steel Cylinder by High Speed Quenching, *Int. Heat Treat. Surf. Eng.*, 2014, **8**(4), p 188–193. https://doi.org/10.1179/1749514814Z.000000000122
99. M.A. Aronov, N. I. Kobasko, and J. A. Powell, Basic Principals, Properties and Metallurgy of Intensive Quenching, SAE Tech. Pap. Ser. 2002-01-1338, March 2002, https://doi.org/10.4271/2002-01-1338
100. N. Kobasko, The Steel Superstrengthening Phenomenon, Part 2, *Int. J. Microstruct. Mater. Prop.*, 2008, **3**(4/5), p 526–547. https://doi.org/10.1504/IJMMP.2008.022034
101. G.E. Totten, N.I. Kobasko, N. Gopinath, and LCF Canale, *Intensive quenching as a viable energy efficient environmentally friendly replacement for carburizing and induction heat treating*, in *International Conference on Advances in Surface Treatment: Research and Applications (SMT XVII and IFHTSE)* (Hyderbad, 2003)
102. M.A. Aronov, N. I. Kobasko and J.A. Powell, *Application of Intensive Quenching Methods for Steel Parts*, in *Proceedings of the 21st ASM Heat Treating Society Conference* (Indianapolis, 2001)
103. M.A. Aronov, N.I. Kobasko, J.A. Powell, J.F. Wallace and Y. Zhu, *Effect of Intensive Quenching on Mechnaical Properties of Carbon and Alloy Steels*, in *Proceedings of the 23rd ASM Heat Treating Society Conference* (Pittsburgh, Pennsylvania, 2005)
104. E. Lyublinski, E.Y. Vaks, N. Kobasko, M. Aronov, and J. Powell, *New Approach for Increasing Corrosion Resistance of Steel, EUROCORR2011 Conf*erence (Stockholm, Sweden, 2011)
105. N.I. Kobasko, Phenomena of Physics Taking Place During Hardening Steel in Water Salt Slution of Optimal Concentration, *Int. J. Phys. Appl.*, 2020, **2**(2), p 6–12.
106. N. Kobasko, Uniform and Intense Cooling during Hardening Steel in Low Concentration of Water Polymer Solutions, *Am. J. Mod. Phys.*, 2019, **8**(6), p 76–85. https://doi.org/10.11648/j.ajmp.20190806.11
107. N. Kobasko, A. Moskalenko and V. Dobryvechir, Research on Use of Low Concentration Inverse Solubility Polymer in Water for Hardening Machine Components and Tools, *Eureka Phys. Eng.*, 2018, **2**, p 63–71. https://doi.org/10.21303/2461-4262.2018.00582
108. N. Kobasko, Research on New Ways of Decreasing Distortion of Steel Parts During Hardening in Liquid Media, *Asian J. Sci. Technol.*, 2017, **8**(8), p 5299–5304.
109. N. Kobasko, Effect of Free Electron in Steel on its Quenching Process in Water and Water Salt Solutions, *Eureka Phys. Eng.*, 2018, **1**, p 39–46. https://doi.org/10.21303/2461-4262.2018.00529
110. M. Beck, C. Schmidt, M. Ahrenberg, C. Schick, U. Kragl and O. Keßler, The Ideal Quenching Medium? Characterisation of Ionic Liquids for Heat Treatment of Metallic Components, *HTM J. Heat Treat. Mater.*, 2013, **68**(5), p 214–223. https://doi.org/10.3139/105.110196
111. M. Beck, C. Schmidt, M. Ahrenberg, C. Schick, U. Kragl and O. Kessler, Ionic Liquids as New Quenching Media for Aluminium Alloys and Steels, *HTM J. Heat Treat. Mater.*, 2015, **70**(2), p 73–80. https://doi.org/10.3139/105.110256
112. C. Schmidt, M. Beck, M. Ahrenberg, C. Schick, O. Keßler and U. Kragl, Room Temperature Ionic Liquids in a Heat Treatment Process for Metals, *RSC Adv.*, 2014, **4**, p 55077–55081. https://doi.org/10.1039/C4RA06901C